Numerical analysis of the Cambridge stratified flame series using artificial thickened flame LES with tabulated premixed flame chemistry

F. Proch[a,*], A.M. Kempf[a,b]

[a] *Institute for Combustion and Gasdynamics (IVG), Chair for Fluid Dynamics, University of Duisburg-Essen, 47048 Duisburg, Germany*
[b] *Center for Computational Sciences and Simulation (CCSS), University of Duisburg-Essen, 47048 Duisburg, Germany*

Abstract

Detailed comparisons of LES results against measurement data are presented for the turbulent lean and rich stratified Cambridge flame series. The co-annular methane/air burner with a central bluff body for flame stabilization has been investigated experimentally by Sweeney et al. [1, 2]. Three cases with varying levels of stratification in the lean and rich combustion regime are taken into account. Turbulent combustion is modeled by using the artificial thickened flame (ATF) approach in combination with flamelet generated manifolds (FGM) lookup tables. The model is adapted for stratified combustion and an alternative formulation for the flame sensor is presented. Three different grids are used to investigate the influence of the filter width and the sub-filter modeling on the overall results. Velocities, temperatures, equivalence ratios, and major species mass fractions predictions are compared with measurements for three different stratification rates and an overall good overall agreement was found between simulation and experiment. Some deviations occur near the bluff body, which are analyzed further by evaluation of atomic and species mass fractions. The stratified combustion process was further investigated and characterized by probability density functions extracted from the simulation results.

Keywords: Turbulent combustion, Stratified combustion, Co-annular jet burner, Large Eddy Simulation, Tabulated chemistry, Cambridge stratified burner

1. Introduction

Premixed combustion plays an important role in modern concepts for gas-turbines and IC-engines because of the reduced pollutant formation. However, to make these systems operable under the lean conditions desired, stratification of the mixture is often required. To predict and optimize the complex interaction between mixing and combustion occuring within these systems, large eddy simulation (LES) has proven to be a suitable and convenient approach.

In contrast to non-premixed combustion, the flame thickness in premixed and stratified combustion processes is normally too small to resolve it properly on a typically LES grid. Different approaches have been developed to overcome this difficulty. One possibility is tracking of the flame front by means of a level-set method. This approach was originally introduced as the G-equation model for Reynolds-averaged Navier-Stokes (RANS) simulations by Peters [3], and later has been adapted to extend its validity to the LES context [4–6].

A second group of models is based on computing the flame structure on the LES grid. In order to properly perform this computation on the too coarse grid, the flame needs to be spatially thickened in the flame normal direction. This can be achieved by reducing the source term and increasing the diffusion term in the transport equations for the chemical species. This technique is referred to as the artificially thickened flame (ATF) [7] approach, which has been successfully applied first in the RANS and later in the LES context [8, 9]. Another possibility is to solve a transport equation for the progress variable and filter it with a filter size larger than the computational mesh, as introduced by Boger et al. [10]. The sum of molecular diffusion and chemical source term for the progress variable is evaluated as a function of the laminar flame speed, similar to the Bray-Moss-Libby model in the RANS context [11]. This method, usually referred to as the flame surface density (FSD) approach, needs modeling of the additional flame surface caused by flame wrinkling on the sub-filter scale level. A wide range of algebraic [12–14] as well as dynamic models have been developed for that purpose, Ma et al. recently presented a detailed study on the subject [15, 16].

A further approach for modeling premixed flames is based on the tabulation of precomputed detailed-chemistry flames. There are two simultaneously developed flamelet-type tabulation strategies for premixed flames, these are the FPI (flame propagation of ILDM) [17–19] and the PFGM (premixed flamelet generated manifolds) [20, 21]. Vreman et al. [22] and later Kuenne et al. [23] combined ATF with PFGM, whereas Galpin et al. [24] extended

*Corresponding author
Email address: fabian.proch@uni-due.de (F. Proch)

the filtered progress variable approach into FPI-PCM (presumed conditional moment), which was further modified by Fiorina et al. [25] resulting in the F-TACLES model.

Recently, these models have been further extended to account for stratified conditions. Different groups have adapted their combustion models for varying mixture fractions inside the lean combustion regime [26–28] to simulate the Darmstadt stratified flame series [29]. Auzillon et al. [30] modified the F-TACLES model for lean stratified combustion and investigated the Darmstadt MOLECULES combustion chamber [31]. Nambully et al. [32, 33] performed LES computations of the Cambridge stratified flame series with the filtered laminar flame (FLF) - PDF model.

The present work aims to continue the investigations on the LES of turbulent stratified flames in the lean and rich combustion regime. The investigated turbulent methane/air burner has recently been developed and investigated at the University of Cambridge and the Sandia National Laboratories by Sweeney, Hochgreb, Dunn and Barlow [1]. Our modeling of turbulent combustion is done by the ATF approach, which is combined with a PFGM tabulation of precomputed premixed flames. Three cases with different levels of stratification are taken into account within this work.

In the first part of the paper, the combustion and subfilter model and the LES-solver are described, pointing at the necessary adaptions to make the approach suitable for stratified combustion over the whole flammability range. A brief description of the experimental setup is also included here. The presentation and discussion of the results starts with a description of the global flame behavior for the different cases investigated. Subsequently, results on different grids are compared to measurements by analyzing radial profiles of mean and rms at different heights above the burner for velocities, equivalence ratio, temperature and species mass fractions. The behavior in the weakly turbulent zone near the bluff body is discussed. After the validity of the approach has been demonstrated, the simulation data is analyzed further to gain a clearer understanding of the influence of different levels of stratification on the flame behavior. For that purpose, probability distributions of relevant quantities are analyzed.

2. Modeling approach

2.1. Generation and accessing of the FGM

In the flamelet generated manifolds (FGM) approach, the chemical state and reaction progress space is tabulated over just a small subset of control variables. This is described only briefly here, the detailed derivation was presented by van Oijen et al. [20, 21]. The basis for the FGM is a set of one-dimensional freely propagating premixed flames, which are computed using a detailed chemical mechanism.

In the present work, these computations are performed using the reaction kinetics library Cantera [34] with the GRI-3.0 [35] mechanism for methane-air flames. The resulting chemical state is tabulated over a progress variable, which is chosen as the sum $Y_C = Y_{\mathrm{CO_2}} + Y_{\mathrm{CO}} + Y_{\mathrm{H_2O}}$ of the major product species mass fractions. We found that this progress variable definition works well for the cases investigated, although more complete formulations surely exist [36, 37].

To make the tabulation suitable for stratified combustion, multiple flames with varying initial gas composition are computed. This assumes that stratified combustion can be described by an ensemble of perfectly premixed flames with different initial compositions. Unity Lewis number assumption for all species is used which results in constant atomic mass fractions over the flame. As the Cantera library normally does not support such unity Lewis number computations, it was modified to compute the transport coefficients for that purpose. It is known that this assumption has a notable influence on the laminar flame speed of methane/air flames for equivalence ratios bigger than approximately 0.8 [38]. Nevertheless, this assumption has turned out to work well in the context of turbulent combustion, and therefore has been and is used by numerous groups in different combustion models with good success [10, 23, 25, 26, 30, 39–41]. The advantage of this assumption is that it is consistent with the applied model for the sub-filter treatment as introduced below, which has been derived based on single-step chemistry with constant Lewis number [9]. Furthermore, the mixture fraction remains constant along the flame, which simplifies the tabulation and avoids an additional source term in the respective transport equation. In the present work, the mixture fraction formulation by Bilger [42] has been used, which is related to the fresh gas equivalence ratio in the following manner:

$$\phi = \frac{Z}{1-Z}\frac{1-Z_s}{Z_s} \tag{1}$$

The stoichometric mixture fraction takes a value of $Z_s = 0.054$. The flammability limits of methane are set to $Z_{fl} = 0.026$ or $\phi_{fl} = 0.45$ and ($Z_{fr} = 0.093$ or $\phi_{fr} = 1.8$) on the lean (rich) side [43, 44]. Outside the flammability limits, a linear interpolation of the species mass fractions and the enthalpy is applied, assuming ideal mixing towards the state of pure air ($Y_{\mathrm{O_2}} = 0.23$, $Y_{\mathrm{N_2}} = 0.77$) and pure fuel ($Y_{\mathrm{CH_4}} = 1$) at ambient conditions. The remaining quantities like temperature, density and transport coefficients can be determined consistently with the thermophysical models used within the flammability limits.

The resulting manifold is stored in a two-dimensional equidistant lookup-table with the mixture fraction Z and the dimensionless progress variable

$$C = \frac{Y_C - Y_C^{min}(Z)}{Y_C^{max}(Z) - Y_C^{min}(Z)} \tag{2}$$

as independent variables, permitting fast non-searching access within the CFD-solver. The FGM includes quantities required by the CFD-solver such as laminar viscosity,

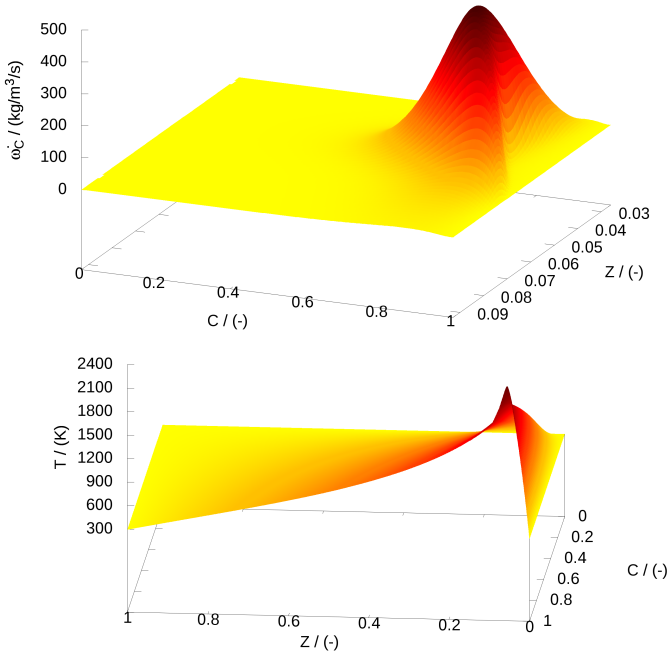

Figure 1: Progress variable reaction rate $\dot{\omega}_C$ and temperature T as function of mixture fraction Z and dimensionless progress variable C. The temperature plot shows the entire mixture fraction range, whereas the illustration of the source term only shows the flammability range, as it vanishes outside.

density or progress variable reaction rate, but also post processing quantities like temperature and species mass fractions. Figure 1 shows the corresponding entries of the table for progress variable reaction rate and temperature. The table is based on 68 premixed one-dimensional flame computations to cover the whole range of flammable mixture fractions, and it has 201 entries in progress variable and 1001 entries in mixture fraction direction.

2.2. ATF approach

In the ATF approach, the flame (typical thickness of $0.1-0.5$ mm) is artificial thickened with the goal of resolving it on a practically affordable LES grid with typical cell sizes bigger than 0.5 mm. This is achieved by introducing a thickening factor F into the Favre-filtered transport equation of the progress variable mass fraction:

$$\frac{\partial \bar{\rho}\tilde{Y}_C}{\partial t}+\frac{\partial}{\partial x_i}\left(\bar{\rho}\tilde{u}_i\tilde{Y}_C\right) = \frac{\partial}{\partial x_i}\left(\left[FE\bar{\rho}D_C+(1-\Omega)\frac{\mu_t}{Sc_t}\right]\frac{\partial \tilde{Y}_C}{\partial x_i}\right)+\frac{E}{F}\dot{\omega}_C \tag{3}$$

In Eq. 3, ρ, u_i, μ_t and Sc_t denote the fluid density, flow velocity, turbulent viscosity and turbulent Schmidt number respectively. The progress variable diffusion coefficient D_C and reaction rate $\dot{\omega}_C$ are obtained from the FGM table. The flame sensor Ω and the efficiency function E are discussed below. The choice of an un-normalized progress variable, also applied in other works (e.g. [26, 30]), avoids cross terms which would occur for a normalized progress variable, e.g. the cross-scalar dissipation rate term.

In contrast to the classical formulation of the ATF model [9], the thickening factor F is only applied inside the flame region, which is characterized by a high gradient of the progress variable, as suggested by Legier et al. [45]. The thickening factor is reduced smoothly to unity outside the flame region to avoid unphysical behavior in regions of pure mixing as well as excessive and unnecessary thickening of the pre-heat and burnout zones. The detection of the flame region is performed by the flame sensor Ω, which takes a value of zero in fully burnt or unburnt regions and increases up to unity inside the flame. It should be mentioned that the ATF method without a flame sensor is also able to recover the correct flame propagation. However, the flame sensor improves the method by ensuring that the (unphysical) thickening of the flame is limited to the regions where it is numerically necessary. This especially avoids an unphysical spatial extension of the burnout zones, which is of particular importance near the bluff body of the investigated burner. Our investigations have shown that with the use of a constant thickening factor, the burnout zones interfere in this region on the coarse grid, causing an extinction of the flame (which does not represent the physical behavior). With the flame sensor, simulations on the coarse grid were possible without problems. A study of the impact of the flame sensor on the medium grid can be found in Appendix A. A common choice for the flame sensor Ω is based on the progress variable, as suggested by Durand and Polifke [46]:

$$\Omega(C) = 16\left[C\left(1-C\right)\right]^2 \tag{4}$$

In this work, the normalized gradient of the progress variable from the one-dimensional Cantera flame computations is used instead. It is mapped over progress variable and mixture fraction and stored as an additional quantity inside the FGM table.

$$\Omega(C,Z) = \left[\frac{\frac{dY_C(x)}{dx}}{\max\left(\frac{dY_C(x)}{dx}\right)}\right]_{1-D} \tag{5}$$

The advantage of this choice is that the thickening behavior becomes independent of the local mixture fraction, as illustrated in Fig. 2. Shown are the profiles of dimensionless progress variable C and the two flame sensors computed with equations 4 and 5 as a function of the flame coordinate normalized by the laminar flame thickness δ_l^0. The laminar flame thickness is based on the temperature profile

$$\delta_l^0 = \frac{T_b - T_u}{\max\left(\frac{dT}{dx}\right)}\ , \tag{6}$$

where the subscripts b and u denote the burnt and unburnt state, respectively. To compare the flame sensors for the whole mixture fraction range, plots are shown for

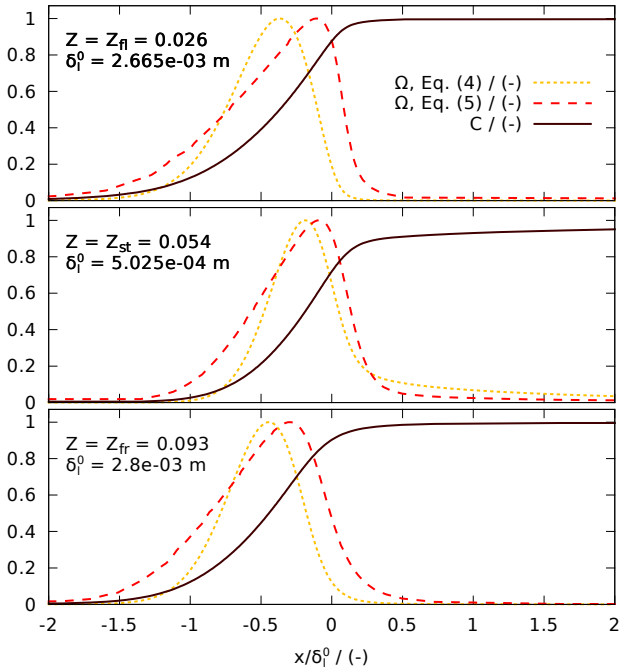

Figure 2: Comparison of profiles of the progress variable C and two different flame sensors Ω over the normalized flame coordinate. Compared are plots for stoichometric (Z_{st}) conditions and the lean (rich) flammability limit Z_{fl} (Z_{fr}).

the stoichometric condition, the lean and the rich flammability limit. The gradient based sensor covers the entire C-profile, independent of the mixture fraction value. The C based sensor also works sufficiently well for stoichometric conditions, but rarely covers the high-temperature part of the flame at both flammability limits. This leads to an inconsistent thickening procedure inside regions of stratified combustion, which involves the danger of altering the results in an unphysical way.

The final formulation of the thickening factor is:

$$F = 1 + \Omega\,(F_{max} - 1) \tag{7}$$

with

$$F_{max} = \max\left(\frac{n\Delta_{mesh}}{\delta_l^0}, 1\right) \tag{8}$$

Here, Δ_{mesh} denotes the cell size of the computational grid and n represents the number of grid-points to resolve the flame thickness, which was set to 5 as suggested by Charlette et al. [9]. The limitation of F_{max} to unity ensures that the flame is not 'thinned' when the grid is sufficiently fine. As the thermal flame thickness δ_l^0 depends on the mixture fraction, it also needs to be tabulated to ensure a consistent thickening procedure in stratified flames.

The modeling of the effect of turbulent velocity fluctuations at the sub-filter level on the progress variable transport also depends on the flame sensor. Inside the flame, the efficiency function E, which corrects for the loss of flame wrinkling by the ATF-approach is evaluated from the commonly used analytical model of Charlette et al. [9]. This model has been chosen as it improves the original formulation by Colin et al. [8] and avoids unphysical stretching of the flame in regions of low turbulence, as found next to the bluff body. The model is used in the modified version by Wang et al. [47]:

$$E = \left(1 + \min\left[F_{max} - 1, \Gamma_\Delta\left(F_{max}, \frac{u'_\Delta}{s_l^0}, Re_\Delta\right)\frac{u'_\Delta}{s_l^0}\right]\right)^\beta \tag{9}$$

This formulation makes the model suitable for finer grid resolutions, as the original model implicitly assumed that $F_{max} \gg 1$ (F_{max} takes values between 2.5 and 10 within this work). In Eq. 9, s_l^0 denotes the laminar flame speed, which is obtained from a table lookup depending on the mixture fraction, F_{max} is determined with Eq. 8. The model constant is set to the common value of $\beta = 0.5$, which was proposed by Charlette et al. [9] and is also used by other groups [26, 30]. The complete formulation of the remaining terms in Eq. 9 can be found in Appendix B. Outside the flame region the sub-filter fluxes are modeled by the eddy diffusivity approach, it is smoothly blended over by use of the flame sensor as shown in the first term on the RHS of Eq. 3.

2.3. Sub-filter closure

As described above, in the FGM approach for stratified combustion the computational quantities are determined from a table lookup depending on mixture fraction and progress variable. However, inside the LES simulation only the filtered values of the independent variables are available. To account for the unknow sub-filter distribution, a common approach is to assume an analytic shape for it and determine the filtered FGM quantities from:

$$\tilde{\Phi} = \int_C \int_Z \Phi(C,Z) P(C,Z)\; dZ dC \tag{10}$$

The joint sub-filter distribution of progress variable and mixture fraction is represented by the filtered density function (FDF), $P(C,Z)$. A common simplification in modeling of stratified combustion is the assumption of statistical independence of C and Z, which is motivated by the observation that C usually varies on significantly smaller length scales than Z. The consequence is that the local flame front is only exposed at most to a small variation of mixture fraction, in contrast to the high variation of progress variable. It is then possible to rewrite Eq. 10 to:

$$\tilde{\Phi} = \int_C \int_Z \Phi(C,Z) P(C) P(Z)\; dZ dC \tag{11}$$

$$= \int_C P(C) \left(\int_Z \Phi(C,Z) P(Z)\; dZ\right) dC \tag{12}$$

$$= \int_Z P(Z) \left(\int_C \Phi(C,Z) P(C)\; dC\right) dZ \tag{13}$$

The FDF of the respective quantity in the outer integration is approximated by a Dirac delta function (the validity

of this assumption is discussed below):

$$\tilde{\Phi} \approx \int_Z \Phi(C,Z)P(Z)\ dZ \tag{14}$$

$$\approx \int_C \Phi(C,Z)P(C)\ dC \tag{15}$$

In this work, the mixture fraction and progress variable FDF shape is assumed to follow a top-hat distribution as suggested by Floyd et al. [48] and applied with good success to the simulation of a gas turbine model combustor by Olbricht et al. [49]. Vreman et al. [50] carried out a comparison of LES results with different FDFs against DNS data, and found a comparable performance of a top-hat function applied in space to the standard β FDF. The top-hat FDF then avoids the necessity for adding an additional dimension to the FGM table [48, 49], thus reducing the memory requirement and improving the performance of the table lookup. Furthermore, the top-hat FDF is able to represent three-stream mixing in the LES-context, which occurs in the investigated burner between the coflow air and the inner/outer stream, an extensive discussion on the subject and on the comparison of top-hat FDF and β FDF can be found in [48].

To determine the upper (lower) limit of the top-hat FDF for mixture fraction and (if required) progress variable, previous studies [48, 49] computed the value at the cell center plus (minus) the scaled square root of sub-filter variance evaluated from a gradient model like the one by Branley and Jones [51]. Besides introducing the necessity to determine an additional modeling constant, this also causes the problem of handling situations in wich the computed limit falls outside of the valid mixture fraction and normalized progress variable range between zero and unity.

To avoid this problem, within this work the value of the filtered quantities is determined from the average of two top-hat distributions, one ranging from the minimum value on the cell faces to the value at the cell center and the second between the cell center value and the maximum value on the cell faces. The face values are determined by linear interpolation between the neighboring cell centers. It is shown in Appendix C that this converges to the gradient formulation for the case of a linear one-dimensional mixture fraction profile over the cell, the same holds for the normalized progress variable. For cases with curved mixture fraction (normalized progress variable) profiles the order of the approximation is improved in comparison to the gradient formulation.

To investigate the influence of sub-filter modeling, the following coarse grid simulations have been carried out for all three cases: a simulation with a Dirac delta function in C and a top-hat FDF in Z (LES-C-SZ), a simulation with a Dirac delta function in Z and a top-hat FDF in C (LES-C-SC), and finally a simulation with Dirac delta functions in both Z and C (LES-C). As shown in the discussion of the results below, it turned out that the sub-filter modeling has only a small influence on the results for the investigated configurations. Therefore, the medium and fine grid computations have been performed with the assumption of a Dirac distributions for both progress variable and mixture fraction, as the sub-filter contribution can be expected to be smaller on the finer grids.

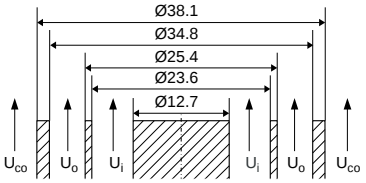

Figure 3: Sketch of the burner setup, all dimensions in mm.

Table 1: Operating conditions of the burner for the different cases. Shown are mean axial velocities, ambient temperature and equivalence ratios.

Case	U_i	U_o	U_{co}	T	ϕ_i	ϕ_o	ϕ_{co}
	m/s	m/s	m/s	K	-	-	-
SwB1	8.31	18.7	0.4	295	0.75	0.75	0
SwB5	8.31	18.7	0.4	295	1.0	0.5	0
SwB9	8.31	18.7	0.4	295	1.125	0.375	0

3. Experimental and numerical setup

3.1. Experiment

The Cambridge stratified burner [1] consists of two annular slots surrounding a central bluff body. Each slot supplies a perfectly premixed methane/air mixture with varying composition allowing to investigate different levels of stratification. The burner is embedded in a coflow of air. A sketch of the setup is shown in Fig. 3. Three different stratified cases are investigated here. Table 1 summarizes the corresponding operating conditions. The resulting Reynolds numbers are 5,960 in the inner and 11,500 in the outer stream. Based on measured values [1] of $u' = 4.37$ m/s and $L_{turb} = 1.72$ mm for the intensity and length scale of the turbulent fluctuations 45 mm downstream of the burner exit, the combustion process falls into the thin reaction zone regime of the modified Borghi diagram for the whole range of equivalence ratios. Velocity data is available from PIV- and LDA-measurements by Zhou et al. [52], the latter ones used as reference in this work. This choice is based on the availability of LDA data at all scalar measurement locations, whereas the PIV data is only available up to 60 mm. Radial profiles for temperature and mass fractions of major species are available from Rayleigh respectively Raman scattering measurements by Sweeney et al. [1].

3.2. CFD-solver and numerical setup

The numerical simulations have been performed with the in-house LES-code 'PsiPhi' [27, 53, 54]. The program

solves the low-Mach number Favre-filtered governing equations for mass, momentum, progress species and mixture fraction. Continuity is ensured by a projection method, the resulting Poisson equation for pressure is solved iteratively by the Gauss-Seidel method with successive over-relaxation (SOR). The equations are discretized with the finite-volume method (FVM) on an equidistant and orthogonal cartesian grid. Interpolation of the convective fluxes on the cells faces is performed by a second order central-difference scheme for momentum and a total variation diminishing (TVD) scheme with non-linear CHARM limiter [55] for density and other scalars. The solution is advanced in time with a low-storage third order Runge-Kutta scheme. The code is parallelized with a distributed memory domain decomposition concept using the message passing interface (MPI). The method of immersed boundaries is applied for a computationally efficient treatment of the geometric shape.

The effect of the velocity fluctuations at the sub-filter level is modeled with the eddy-viscosity approach for momentum and the eddy-diffusivity approach for mixture fraction and progress variable, with the turbulent Schmidt number set to 0.7. The turbulent viscosity is evaluated with the σ-model suggested by Nicoud et al. [56]:

$$\mu_t = \rho \left(C_m \Delta\right)^2 D_m \left(\tilde{u}\right) \tag{16}$$

In this model, the differential operator D_m is a function of the singular values of the velocity gradient:

$$D_m = \frac{\sigma_3 \left(\sigma_1 - \sigma_2\right) \left(\sigma_2 - \sigma_3\right)}{\sigma_1^2} \tag{17}$$

with

$$\sigma_1 \geq \sigma_2 \geq \sigma_3 \geq 0 \tag{18}$$

The singular values σ_i are identically equal to the square root of the eigenvalues of the tensor:

$$G_{ij} = \frac{\partial \tilde{u}_k}{\partial x_i} \frac{\partial \tilde{u}_k}{\partial x_j} \tag{19}$$

The corresponding modeling constant is set to a value of $C_m = C_\sigma = 1.5$. The σ model has been chosen as it avoids the over-prediction of the turbulent viscosity near walls and in shear layers typical of the classical Smagorinsky model without using a computational expensive dynamic procedure.

The computational domain extends 112 mm in the axial z-direction, and 110 mm in the x- and y-directions. The last 12 mm of the burner have been included in the simulation to obtain realistic flow conditions at the burner exit. To study the influence of filter width on the results, computations have been carried out for three different grid resolutions, which are summarized with the respective computational costs in Table 2. The sampling for statistical means and variances was started after 7 and carried out for at least 8 flow-trough times based on the inner stream velocity, leading to a simulated time of approximately 0.2 seconds.

Table 2: Details of the simulations on three different grids. The computations were run for 15 flow through times at the inner stream velocity $U_i = 8.31$ m/s.

Grid	Δ_{mesh} mm	n_{Cells} million	t_{CPU} h	t_{Wall} h	n_{Procs} -
Coarse (C)	1.0	1.6	91	2.5	36
Medium (M)	0.5	13.4	3,533	10.3	343
Fine (F)	0.25	103.2	49,152	96.0	512

Parabolic velocity profiles with mean values corresponding to Table 1 and superimposed pseudo-turbulent fluctuations were set at the inflow of the computational domain. The fluctuations were generated with the filtering method of Klein et al. [57] in an efficient numerical implementation proposed by Kempf et al. [58]. The turbulent length scale was set to 1 mm and the rms of the fluctuations to 2.5 m/s. A zero gradient condition was imposed at the outflow for all quantities.

4. Results and discussion

4.1. General flame behavior

Figure 4 shows instantaneous and mean simulated contour plots of equivalence ratio in a burner cross section, giving a first impression of the flow. Downstream of the burner exit, mixing occurs between the coflow and the outer stream in all three cases and in addition between the inner and outer stream in the SwB5 and SwB9 cases. The mixing rate is increased by additional turbulent motion developing in the shear layers between the coflow and the inner and outer stream. The lean flammability limit is denoted by a black isoline, which starts between the outer stream and the coflow at the burner exit and slowly widens up further downstream for SwB1 and SwB5. For SwB9 the mixture of the outer stream is leaner than the flammability limit, therefore the isoline starts between the inner and outer stream and widens up to a smaller radius than in the other cases. The isolines of the flame sensor (Eq. 5), which border the region where combustion takes place, are shown in white.

One can distinguish three characteristic flame regions. The first region is perfectly premixed and characterized by a constant mean flame angle and only moderate broadening of the mean flame brush.

The second region starts where the (instantaneous) flame enters into the region of equivalence ratio gradients, and is exposed to stratification. The curvature decreases (increase) for the isolines of the mean flame sensor at the unburnt (burnt) side of the flame, resulting in a broadening of the mean flame brush. This location is found at approximately 40 mm (SwB1), and 30 mm (SwB5, SwB9). In addition, from about 40 mm onwards the whole flame is

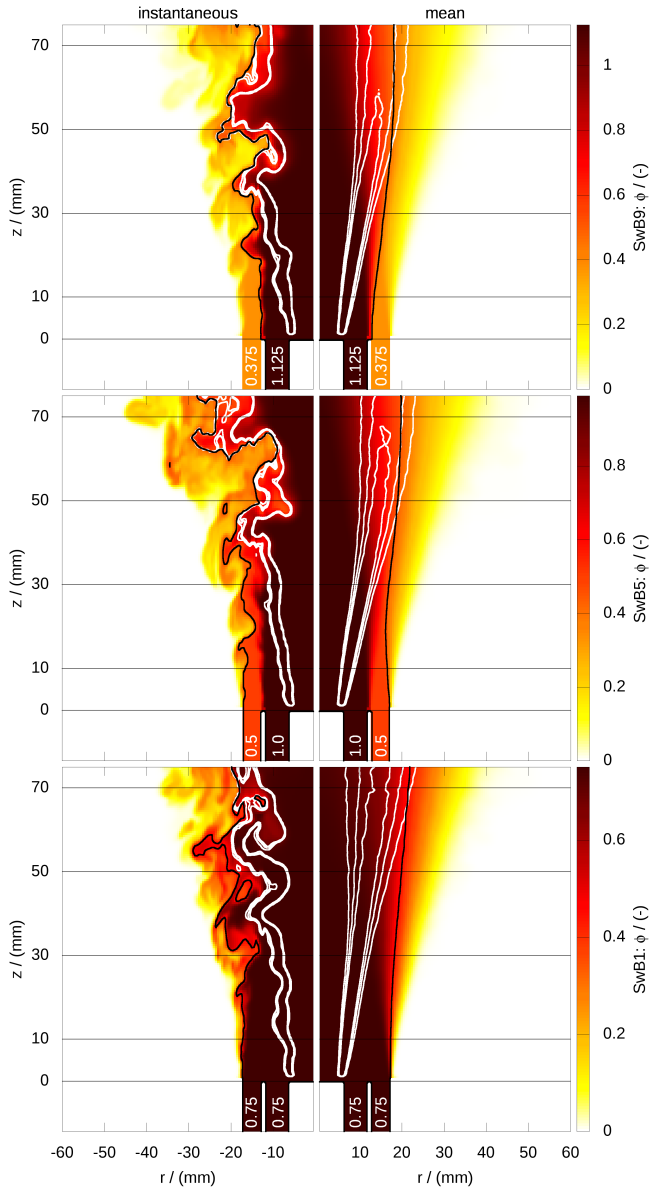

Figure 4: Instantaneous and mean contour plots of equivalence ratio in a burner cross section for the three investigated cases on the medium grid, the lean flammability limit is marked by a black isoline, the flame sensor which marks the combustion region is denoted by white isolines. The values in the nozzle give the respective equivalence ratio.

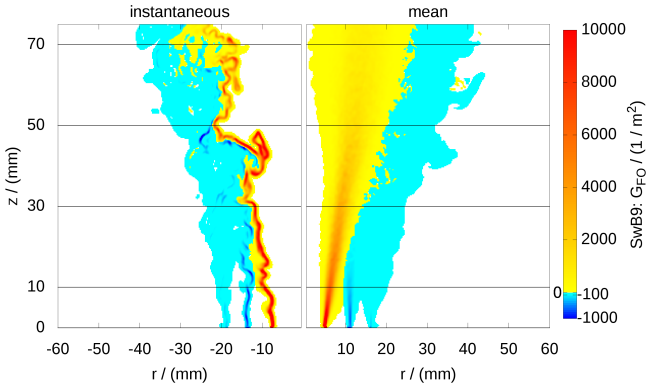

Figure 5: Instantaneous and mean contour plots of the flame index in a burner cross section for SwB9. Values between -0.1 and +0.1 are colored in white.

exposed to an equivalence ratio gradient in the two latter cases. The equivalence ratio at the burnt side of the flame converges then towards a value of 0.6, which is the mean of the value at the flammability limit and the average value at the inlet, which is 0.75 for all cases.

The transition point to the third region is located where the instantaneous flame touches the flammability limit line. Here, the motion of the unburnt side of the flame is determined by the mixing behavior and the outer isoline of the flame sensor coincides with the flammability limit. In contrast to before, the curvature of the isolines of the mean flame sensor increases at the unburnt side of the flame and decreases at the burnt side of the flame resulting in a decrease of the flame angle and a stabilization of the flame brush thickness. This region starts at around 60 mm (SwB1), and 50 mm (SwB5, SwB9).

To demonstrate that the premixed mode is dominant, Fig. 5 shows instantaneous and mean contour plots of the flame index evaluated from [19, 59]:

$$G_{FO} = \nabla Y_{CH4} \cdot \nabla Y_{O_2} \tag{20}$$

Only the results for the mostly stratified case SwB9 are displayed as the results are comparable for the other cases. The flame index takes positive (negative) values in premixed (non-premixed) regions and becomes zero outside of the reaction zone. Overall the combustion process takes places in a premixed environment. Only in very small regions at the unburnt side of the instantaneous reaction zone the flame index becomes slightly negative locally.

4.2. Velocities

Comparisons of mean and rms radial profiles of axial and radial velocity components from simulations and experiments for all three cases are shown in Figures 6-9. The LDA measurements from Zhou et al. [52] are denoted by black dots. For the coarse grid two additional data sets are shown (LES-C-SZ and LES-C-SC), which were obtained with sub-filter modeling using the top-hat FDF, as explained in section 2.3. For all cases the impact of

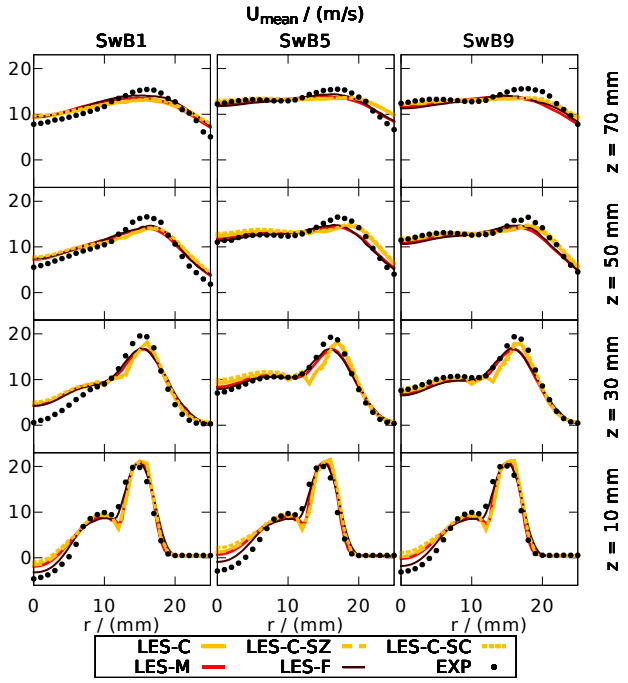

Figure 6: Radial profiles of the mean axial velocity at different downstream locations, showing a comparison for three different grids with the experiments. LES-C-SZ and LES-C-SC refer to a coarse grid simulation with additional sub-filter modeling using a top-hat FDF in mixture fraction and progress variable, respectively.

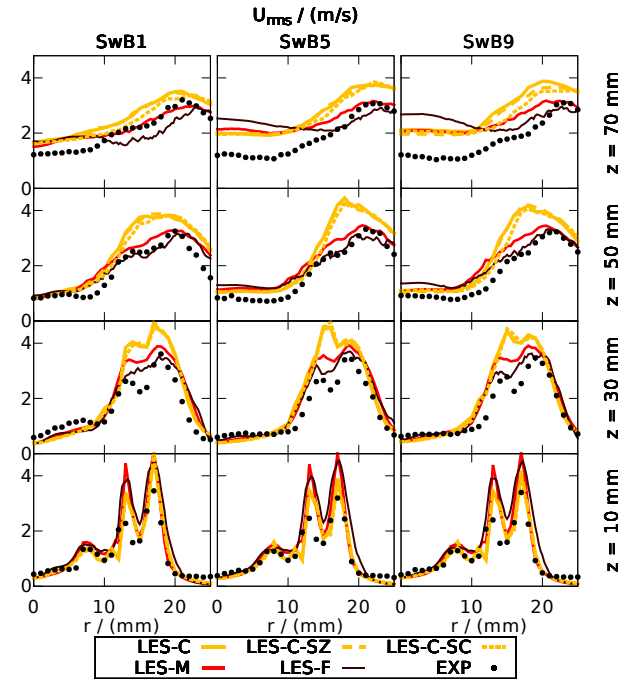

Figure 7: Radial profiles of the axial velocity fluctuations at different downstream locations, showing a comparison for three different grids with the experiments. LES-C-SZ and LES-C-SC refer to a coarse grid simulation with additional sub-filter modeling using a top-hat FDF in mixture fraction and progress variable, respectively.

the bluff body and the different velocity magnitudes on the flow field are clearly visible. In the region behind the bluff body a recirculation zone is formed, which disappears further downstream due to momentum exchange with the faster inner flow and thermal expansion. The latter phenomenon is more dominant for SwB5 and SwB9, as the zone of the flame with strong reaction is shorter in these cases, as can be seen from the isolines of the flame sensor in Fig. 4. In the shear layers between the streams and the coflow the turbulent fluctuations are amplified.

The simulation results are in good agreement with the experiments, the basic trends are matched for all cases and grid resolutions. The quality of the predictions improves with grid refinement, here the differences between the coarse and medium grid are bigger than between the medium and fine grid, implying good convergence. The agreement of the fluctuations with the measurements benefits substantially from the refinement of the grid. The influence of the top-hat sub-filter model on the coarse grid velocity results is generally small. Slight deviations occur for the fluctuations of axial velocity at the last two measurement positions, where also the agreement with the experimental results declines for all cases and grids. This can be attributed to the size of the computational domain, which was chosen to be compact so that fine grid simulations are computationally affordable. (To investigate the influence of the domain size, additional simulations on the coarse grid with doubled domain size in all directions have been performed for all three cases. It was found that the influence of the domain size is negligible for the means of all investigated quantities and the fluctuations of all quantities except for axial velocity at the last two measurement positions. The respective comparisons can be found in Appendix D.)

The strength of the recirculation zone is under predicted by the simulation, most visible for SwB1. This is in agreement with simulation results by Nambully et al. [32], and might be an indicator that the flame is slightly lifted at the bluff body, which can not be reproduced with the applied adiabatic combustion model. However, this affects only a limited area of the flow field and has no significant influence on the regions of interest, which are the regions where (stratified) combustion occurs.

The radial velocity component shows a considerable deviation towards the center line where the measurements show a negative velocity, whereas the simulations predict zero velocity. This suggests that the experimental data is slightly asymmetric, which on the one hand could be due to measurement uncertainties caused by the small magnitude of the quantity. On the other hand, such burner configurations are known to be highly sensitive to small deviations in the geometrical shape, so that the measured asymmetry may represent the real flow field. This (unwanted) asymmetry is very hard to take into account within a numerical simulation, and again the effect on the rest of the flow field is small. Overall the flow field is well captured by the simulation, which is a prerequisite for the correct prediction

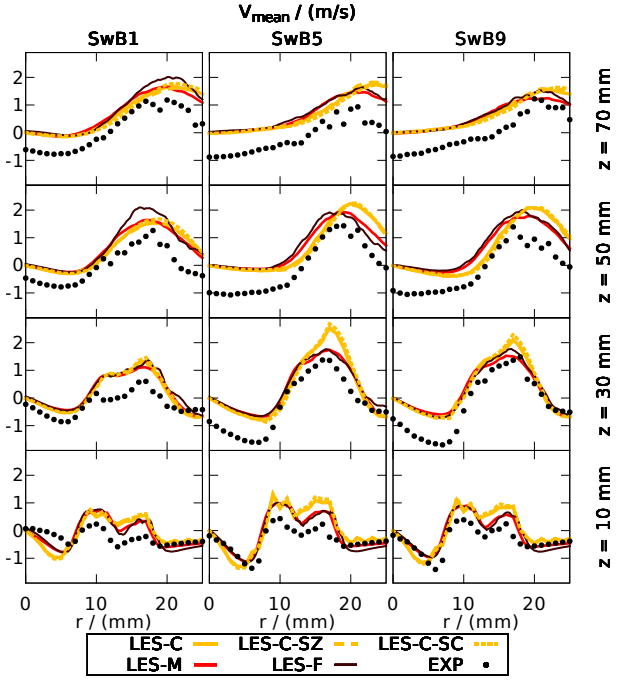

Figure 8: Radial profiles of the mean radial velocity at different downstream locations, showing a comparison for three different grids with the experiments. LES-C-SZ and LES-C-SC refer to a coarse grid simulation with additional sub-filter modeling using a top-hat FDF in mixture fraction and progress variable, respectively.

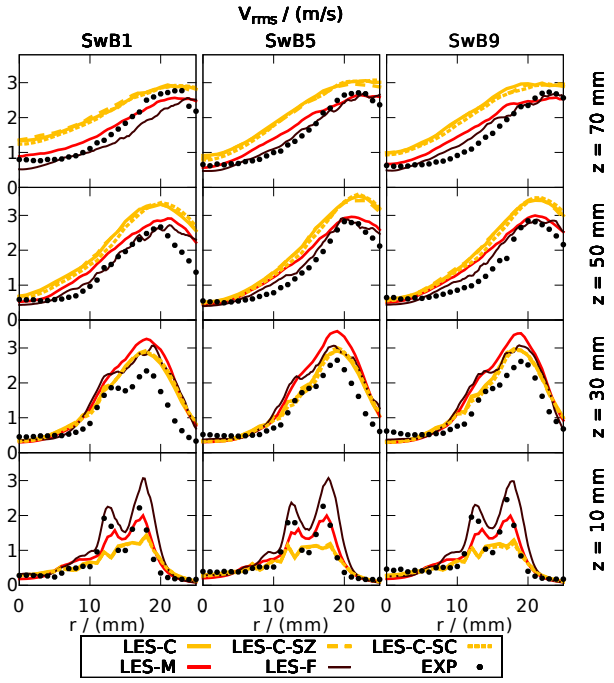

Figure 9: Radial profiles of the radial velocity fluctuations at different downstream locations, showing a comparison for three different grids with the experiments. LES-C-SZ and LES-C-SC refer to a coarse grid simulation with additional sub-filter modeling using a top-hat FDF in mixture fraction and progress variable, respectively.

of scalar quantities.

4.3. Equivalence ratio, temperature and progress variable

The comparisons of mean and rms profiles of equivalence ratio and temperature against the measurements by Sweeney et al. [1] are shown in Figures 10-13. The profiles of the equivalence ratio mirror the observations made for the flow field. The steep gradients between the inner and outer streams and the coflow are dissipated downstream, and fluctuations are produced within the shear layers in between. The behavior of the temperature profiles correlates strongly with the observations made for the mean flame brush in Fig.4, as expected for a unity Lewis number assumption. The basic trends from the measurements are matched by the simulations, and the effect of grid refinement and sub-filter model is comparable to the observations made for velocities.

The mean Favre-filtered normalized progress variable is also shown for completeness in Fig. 14. The progress variable profiles are comparable to the temperature profiles, which was to expected for a unity Lewis number assumption. The strong effect of the efficiency function is shown in Fig. 14, which also includes profiles that were obtained from additional simulations with the efficiency function set to unity inside the whole domain. It becomes obvious that, although the Reynolds numbers are small in the investigated burner, taking into account the loss of flame wrinkling by the thickening procedure is crucial for the correct flame propagation. This is also reflected by

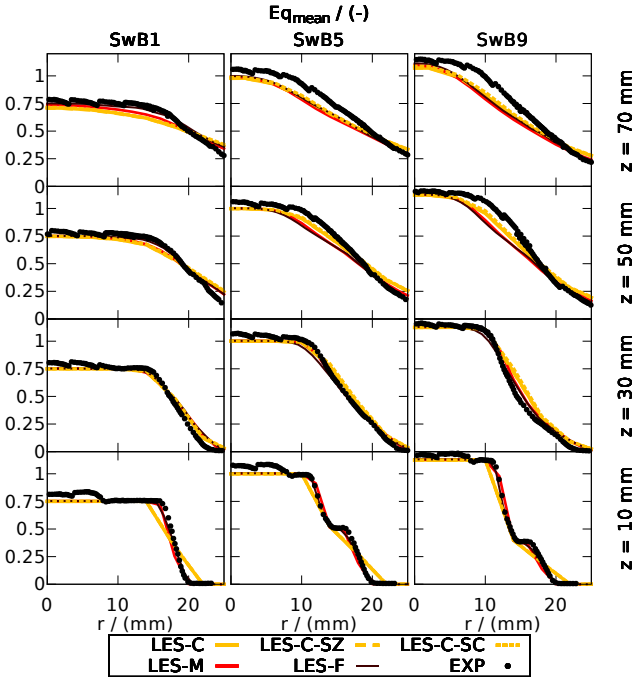

Figure 10: Radial profiles of the mean equivalence ratio at different downstream locations, showing a comparison for three different grids with the experiments. LES-C-SZ and LES-C-SC refer to a coarse grid simulation with additional sub-filter modeling using a top-hat FDF in mixture fraction and progress variable, respectively.

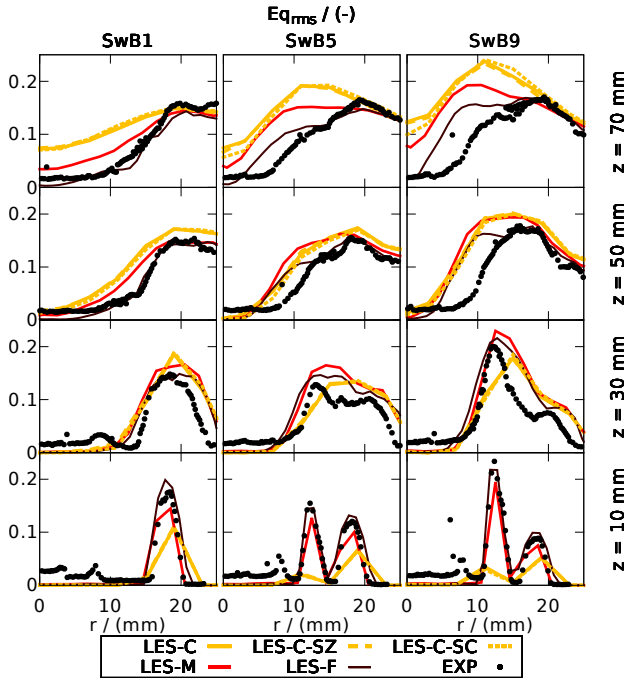

Figure 11: Radial profiles of the equivalence ratio fluctuations at different downstream locations, showing a comparison for three different grids with the experiments. LES-C-SZ and LES-C-SC refer to a coarse grid simulation with additional sub-filter modeling using a top-hat FDF in mixture fraction and progress variable, respectively.

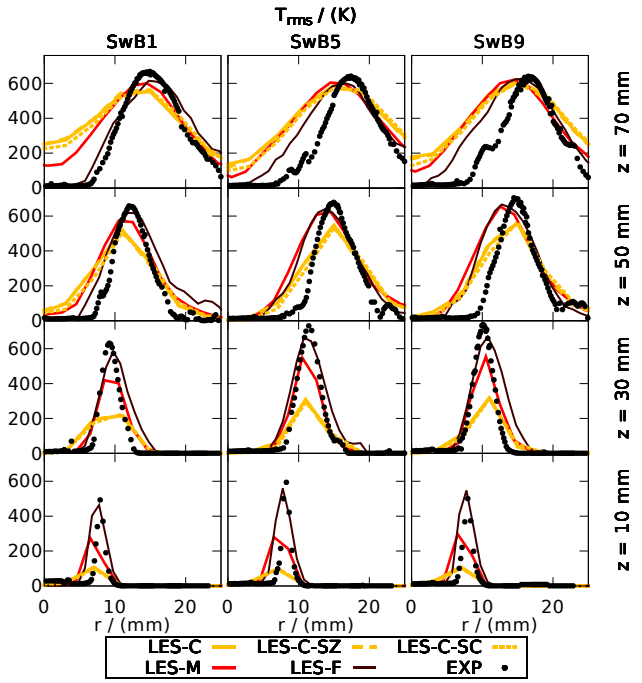

Figure 13: Radial profiles of the temperature fluctuations at different downstream locations, showing a comparison for three different grids with the experiments. LES-C-SZ and LES-C-SC refer to a coarse grid simulation with additional sub-filter modeling using a top-hat FDF in mixture fraction and progress variable, respectively.

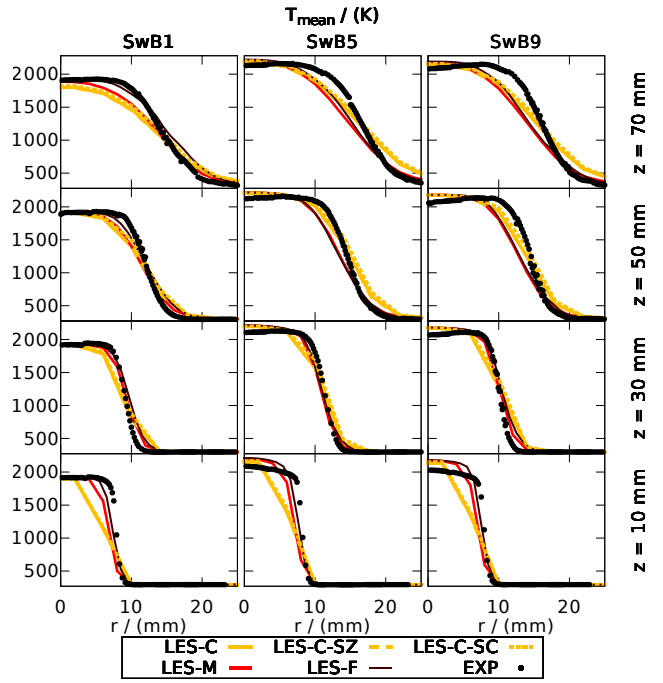

Figure 12: Radial profiles of the mean temperature at different downstream locations, showing a comparison for three different grids with the experiments. LES-C-SZ and LES-C-SC refer to a coarse grid simulation with additional sub-filter modeling using a top-hat FDF in mixture fraction and progress variable, respectively.

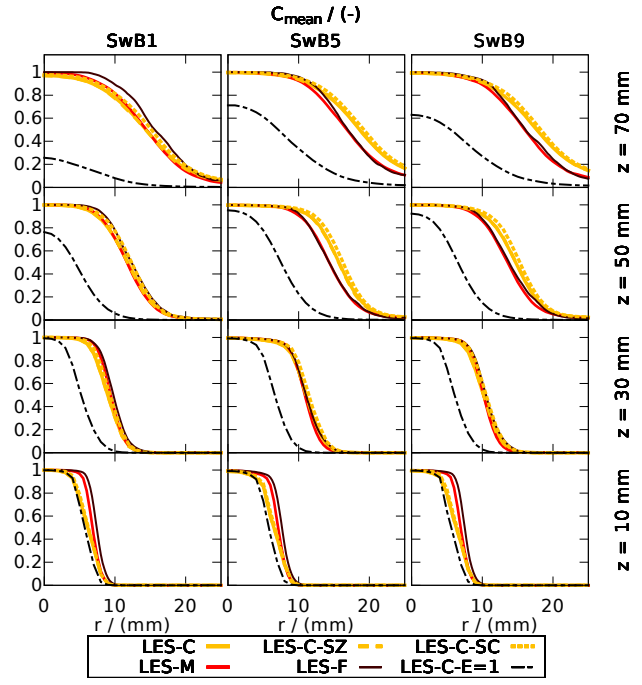

Figure 14: Radial profiles of the mean Favre-filtered progress variable at different downstream locations. LES-C-SZ and LES-C-SC refer to a coarse grid simulation with additional sub-filter modeling using a top-hat FDF in mixture fraction and progress variable, respectively. LES-C-E=1 shows the results of a computation without efficiency function, i.e. setting $E = 1$ in Eq. 3.

the magnitude of the efficiency function observed in the simulations, which lies around three for the coarse grid.

To get a better understanding of the reason why the effect of the mixture fraction sub-filter model is negligible, Fig. 15 shows the instantaneous maximum and minimum mean Favre-filtered mixture fraction values at the faces for one time step. In the vast majority of cells, the mixture fraction varies by less than 10% of the stoichometric value between the cell center and the faces, the corresponding range is marked by thin dark-red lines in Fig. 15. To check the possible influence of this range on the flame propagation, Fig. 16 shows the laminar flame speed over the mixture fraction as used in the simulation. The spacing of the mixture fraction grid lines corresponds also to 10% of the stoichometric value. Assuming an adequately resolved (thickened) progress variable field, it is notable that a piecewise-linear approximation with this mixture fraction sub-filter variance, which corresponds to a computation with the top-hat sub-filter model, is able to reproduce the flame speed correlation with a small error, even around the stoichometric region with high curvature values. At the same time, an approximation by the value at the center of each interval, which would correspond to the assumption of a Dirac peak for the sub-filter distribution, would lead to an almost identical result. In other words, the impact of the sub-filter model is very small. This is in agreement with the findings of Cavallo Marincola et al. [27].

However, Fig. 15 shows some distinct features which could become important for other cases with higher sub-filter variance. First, the plot is not perfectly symmetric, as would be implicitly assumed by a gradient model for the sub-filter variance. There even exist some points where the mixture fraction has a local maximum or minimum at the cell center, which is denoted by minimum (maximum) values of $\tilde{Z}$ at the cell faces above (below) the diagonal (in Fig. 15, this is shown by red squares below and yellow triangles above the diagonal line). A second notable feature is the presence of a gap between the diagonal and the mixture fraction points towards higher values of the mixture fraction. This gap is shifted towards the minimum mixture fraction values. This implies that the corresponding cell is located in a region where the mixture fraction profile changes mainly towards leaner mixture fractions. Such condition occur at the point where the mixture fraction profiles starts declining from the broad peak at the stoichometric value towards higher radii. In the Fig. 10 this would correspond to a radial position of approximately 12 mm. High mixture fraction variances mainly occur around the burner exit conditions, which correspond to mixture fraction values of 0 for the coflow and 0.0277 (0.054) for the outer (inner) stream. Although the magnitude of the mixture fraction variances at these three locations is comparable, the distribution among minimum and maximum values varies. At $\tilde{Z} = 0$ ($\tilde{Z} = 0.054$) high variances mainly occur for Z_{max} (Z_{min}). A similar behavior is observed for $\tilde{Z} = 0.0277$, where large Z_{max} occur for large $\tilde{Z}$, and small Z_{min} for small $\tilde{Z}$. The reason for that can again be found in the shape of the equivalence ratio profiles: As shown in Fig. 10, at $\tilde{Z} = 0$ ($\tilde{Z} = 0.054$) a steep gradient exists only towards richer (leaner) conditions. In contrast, the value $\tilde{Z} = 0.0277$ marks an inflection point of the equivalence ratio profile and therefore has considerably gradients towards leaner as well as richer conditions.

The mean temperature profile deviates notably near the bluff body for the coarse grid, which can be explained by the ATF-modeling: The real flame is very thin at the edge of the bluff body due to wall effects, but the ATF approach thickens the flame also at this position to the adjusted 5 grid points according to Eq. 8. To enforce the thin flame here, the thickening would have to be blocked in the cells near the wall, causing an insufficient resolution of the flame leading to poor numerical accuracy. The origin of this problem is that modeling approaches based on broadening of the flame, by thickening or filtering, mean a certain loss in spatial accuracy, which can cause deviations in the flame position in such situations. However, the fact that the flame position is predicted well further downstream also for the coarse mesh may be seen as evidence that the modeling of the overall flame behavior is not deteriorated significantly by this effect. The rms fluctuations of the temperature are under predicted on the coarse and medium grid up to the middle of the computational domain, which is in agreement with the observations made by Kuenne et al. [26], and is likely to be caused by the effect of the thickening procedure on the flame dynamics.

The equivalence ratio (experimental data) plots show a distinct peak in the bluff body region at a radius lower than 10 mm. This has been investigated closer experimentally by Barlow and coworkers [60, 61] and numerically by Katta and Roquemore [62] and Nambully et al. [33]. The effect is explained by preferential diffusion of H_2O and H_2, which can not be captured with the Lewis number unity assumption applied within this work, but will be analyzed further in the next section. Overall, the simulation results are in good agreement with the measurements for equivalence ratio and temperature.

4.4. Major species

To further access the modeling approach and get deeper insights into the chemical structure of the flame, mean and rms radial profiles of major species obtained from the simulation are compared to measurements [1]. The trend and observations made for temperature and mixture fraction in the last section hold for the species, the respective Figures F.29-F.38 have been moved to Appendix F for brevity.

Figure 17 shows a comparison of mean mass fraction profiles of major species 10 mm above the burner with measurements for the fine grid simulation. The related atomic mass fractions for carbon, hydrogen, oxygen and nitrogen are displayed in Fig. 18. Noticeable differences between simulation and experiment can be observed for radii smaller than 10 mm, which will be addressed next.

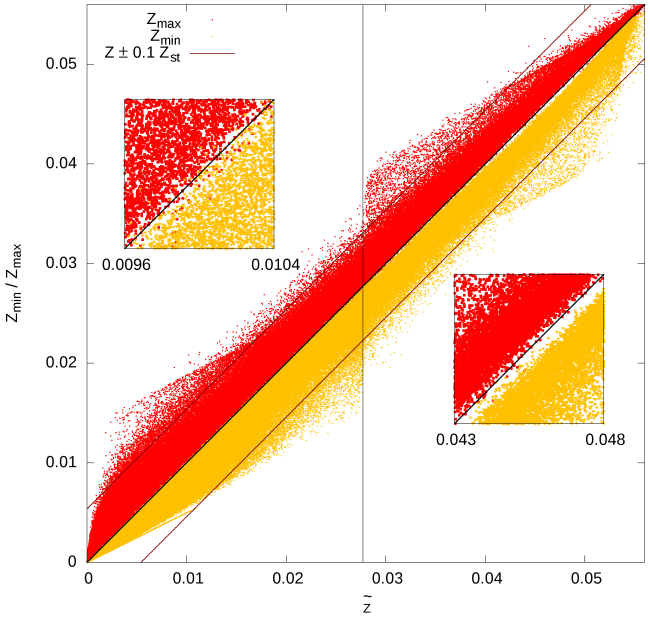

Figure 15: Maximum and minimum mean Favre-filtered mixture fractions at the cell faces as a function of the respective value $\tilde{Z}$ at the cell center for the case SwB5 on the coarse grid with top-hat sub-filter model in Z (LES-C-SZ). The diagonal line corresponds to the values at the cell centers. Enlarged plots are included for regions with distinct features. The range of 10% mixture fraction deviation based on the stoichometric value is bordered by thin lines, the inner stream mixture fraction of 0.277 is marked by a vertical line.

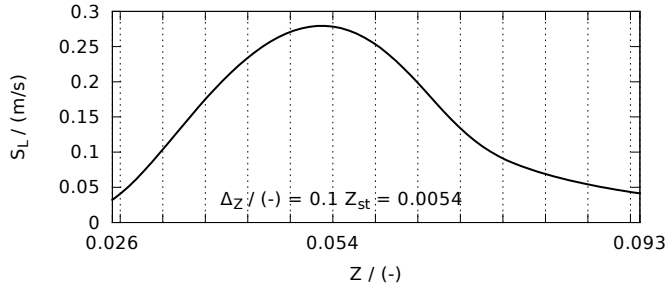

Figure 16: Laminar flame speed vs. mixture fraction for methane/air computed with the GRI-3.0 mechanism and unity Lewis number assumption for all species. The spacing of the mixture fraction grid lines is 10% of the stoichometric value, corresponding to the range indicated in Fig. 15.

For SwB1, the element mass fraction is under predicted for carbon and over predicted for oxygen relative to the experiments. Looking at the species profiles, it can be seen that this corresponds to a lack of CO_2 and a surplus of O_2. The under predicition of carbon also occurs for SwB5 and SwB9, this corresponds to a lack of CO here. For the latter case, an additional over prediction of hydrogen and oxygen can be observed, which can be assigned to a surplus of H_2O.

The under prediction of H_2 mass fraction occurring for all three cases does only have a negligible influence on the atomic mass fraction of hydrogen, as this is dominated by the contributions of H_2O and CH_4. It should be considered that the experimental profiles are somewhat discontinuous for oxygen and nitrogen, where nitrogen shows the inverse behavior of oxygen. In accordance with the observations by Sweeney et al. [1], it is also mentioned here that the agreement of CO_2 measurements with predictions based on one-dimensional flame computations (which are the basis for FGM) is worse than for the other educt and product species (CH_4, H_2O, O_2).

The enrichment of CO_2 in the recirculation zone for SwB1 can be explained with the effect of preferential diffusion suggested by Barlow et al. [60], although the depletion of O_2 is unexpected in that context. In contrast, the enrichment of CO for SwB5 as well as SwB9 and the additional depletion of H_2O for the latter case may be rather due to heat transfer than due to preferential diffusion. One indicator for an heat loss effect is that the measured mean temperature profiles have a remaining slope at the centerline and a lower peak value in comparison to the adiabatic simulation results. Another indicator is that the CO and H_2O mass fractions in the FGM-table for the experimental temperatures at the centerline were found to be in good agreement with the measured concentrations of these species. A non-adiabatic extension of the ATF/FGM model has been presented and applied by Ketelheun et al. [41] with good success, assuming a Dirac peak for the sub-filter distributions.

4.5. Influence of stratification

The effects of stratification on the flame behavior are investigated further. As this is rather thought as a deeper analysis of the combustion process using the capabilities of the numerical simulation than as an additional validation, only the fine grid results are taken into account.

To classify the dependency of the combustion process on the equivalence ratio globally, the normalized PDF of Favre-filtered reaction source term conditional on Favre-filtered equivalence ratio over the entire domain is shown in Fig. 19. To take into account the effects of turbulence and thickening, the last term on the RHS of Eq. 3 was used as the source term. This gives a good representation of the influence that reaction at the given equivalence ratio has on the global combustion process and heat release. The sampling was carried out for at least 8 flow-trough times in accordance with the other flow statistics.

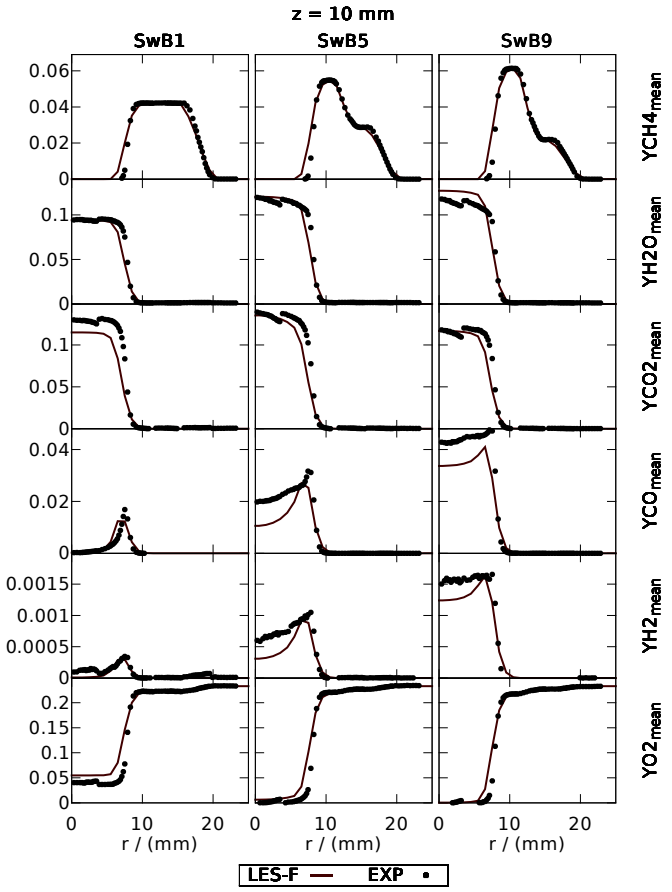

Figure 17: Radial profiles of the mean major species mass fractions 10 mm downstream of the burner exit.

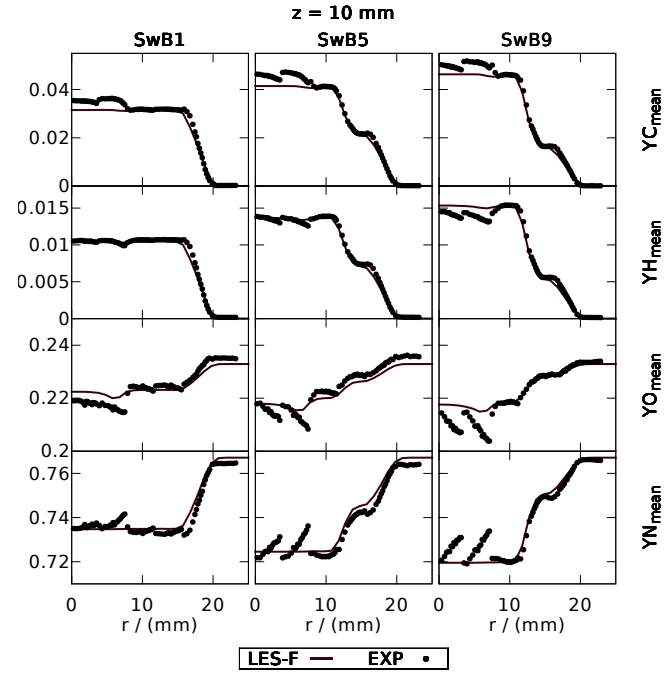

Figure 18: Radial profiles of the mean atomic mass fractions 10 mm downstream of the burner exit

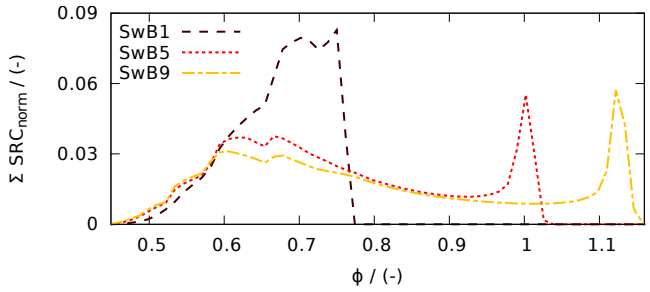

Figure 19: Normalized PDFs of Favre-filtered reaction source term conditional on Favre-filtered equivalence ratio over the entire domain.

For all cases, combustion occurs in the whole range of equivalence ratio between the lean flammability limit and the respective equivalence ratio in the inner stream. Towards the lean flammability limit the reaction probability declines to zero at a comparable rate for all cases.

For SwB1, the PDF is continuously rising until reaching an equivalence ratio of 0.7, followed by a broad peak towards the inner (and outer) stream value of 0.75. This shows that already the presence of an air coflow is sufficient to trigger combustion over the whole equivalence ratio range down to the flammability limit.

For SwB5 and SwB9 the PDF increases steadily from the flammability limit until a value of around 0.6, which corresponds to the burnt side of the flame when it is located completely in a stratified enviroment, as already adressed in section 4.1. From 0.6 onwards, the PDF decreases constantly until it reaches the respective equivalence ratio in the inner stream, here it develops a sharp second peak. The reason why the first peak is much broader than the second one is that the respective samples are found further downstream, where the flame front has been widened by turbulent effects. It is noticeable that the shape of the PDF is very similar for SwB5 and SwB9. The fact that the latter one is partly located within the rich equivalence ratio regime does not seem to have a considerably influence on the stratified combustion process.

Figure 20 shows the normalized joint PDFs of Favre-filtered equivalence ratio against the Favre-filtered flame sensor, the Favre-filtered normalized progress variable and the axial distance from the burner exit. This characterizes the stratified combustion process further taking into account the interaction between the value of equivalence ratio and the intensity of reaction, the reaction progress and the axial position, respectively. Only the points inside the flame region have been considered, the limit has been set at a flame sensor value of 0.01. Therefore the outer stream equivalence ratio does not occur in the axial position plots for small distances, as the flame burns only at the inner stream equivalence ratio in this regions.

The shape of the already discussed reaction source term PDFs is basically mirrored in the joint PDFs of the flame sensor for values near zero, which are found in regions with low reaction rates at the unburnt or burnt side of the

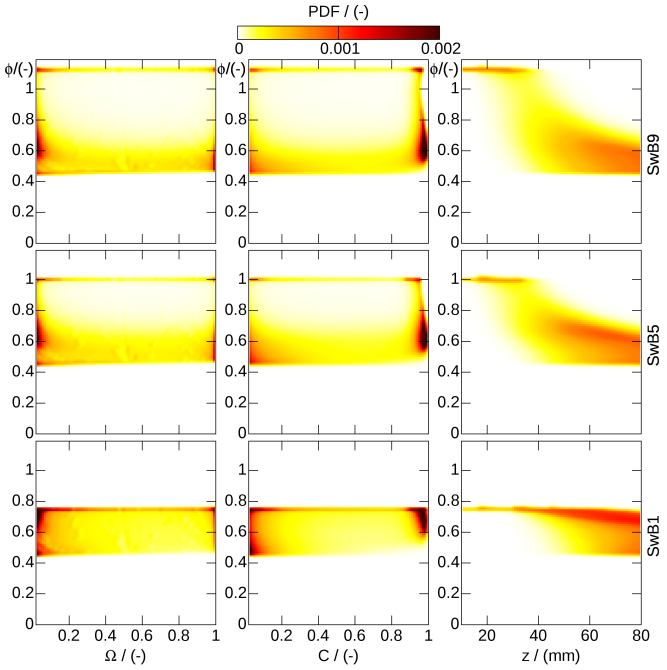

Figure 20: Joint PDFs of Favre-filtered equivalence ratio vs. Favre-filtered flame sensor (left), Favre-filtered normalized progress variable (middle) and distance from the burner exit (right).

flame. For SwB1 the joint PDF shifts towards the inner (and outer) stream equivalence ratio of 0.75 when proceeding to higher flame sensor values. Within the flame zone with the highest reaction rate corresponding to a flame sensor value of unity, most of the combustion is occurring in a broad peak towards the inner (and outer) stream equivalence ratio of 0.75. Nevertheless, contributions of the whole equivalence ratio range are found for all flame sensor values. For SwB1 and SwB5 the bimodal shape with peaks at the respective inner stream equivalence ratio of 1.0/1.125 and the already discussed value of 0.6 gets more and more distinct when proceeding to higher flame sensor values. At a flame sensor value of unity, there is only a negligible amount of samples found in the equivalence ratio range between approximately 0.8 and the inner stream equivalence ratio of 1.0/1.125, which means that for the high reactive part of the flame it can be distinguished between two types of flames which differ about 0.2 respectively 0.3 in equivalence ratio.

Within the progress variable joint PDFs, it can be observed that for SwB1 most of the combustion at equivalence ratios near to the lean flammability limit occurs at low progress variable values near the unburnt side of the flame. At the burnt side of the flame, which is characterized by progress variable values near unity, the combustion process is only exposed to a narrow range of equivalence ratios between approximately 0.6 and 0.75. In contrast to that, combustion towards the lean flammability limit is found within the whole range of progress variable values for SwB5 and SwB9. Progress variable values close to unity are not found for equivalence ratio values larger than approximately 0.75 for the two latter cases. This implies that the respective flames are located further downstream than 40 mm above the burner, as this is the position from where the whole flame is located in a stratified environment, as discussed in section 4.1.

Within the axial position PDFs it can be determined that these two types of flames for SwB5 and SwB9 are also separated spatially, combustion at the inner stream equivalence ratio can be found up to approximately 40 mm. Above this height the flame is burning between the flammability limit and an equivalence ratio of 0.8. The transition between these two regimes takes place relatively rapidly in the region between 25 and 40 mm. This basically correspond to the findings from the analysis of Fig. 4, where three different combustion regimes where found. However, the closer analysis with the joint PDFs has shown that the overall flame behavior is dominated by the contribution of the perfectly premixed combustion (inner stream) and the combustion towards the lean flammability limit (mixing layer between air and outer stream). The contribution of the stratified regime away from the flammability limit between 30 mm and 50 mm is small. For SwB1 the combustion towards the flammability limit starts from around 40 mm onwards, in contrast to the two other cases flames with the inner stream equivalence ratio are dominating troughout the whole domain.

The equivalence ratio value at a point alone is not sufficient to fully characterize the stratified combustion process, as it yields no information on the interaction of the local equivalence ratio gradient with the flame structure. A suitable quantity to investigate this interaction is the alignment angle between the gradients of equivalence ratio and progress variable [26, 27, 63]. It is evaluated for every point in the computational domain according to:

$$\alpha = \arccos\left(\frac{\nabla C \cdot \nabla \phi}{|\nabla C||\nabla \phi|}\right)\frac{180^\circ}{\pi} \ . \qquad (21)$$

The resulting joint PDFs of α versus flame sensor, progress variable and axial position are displayed in Fig. 21. For $\alpha < 90^\circ$, the flame propagates towards lower values of equivalence ratio, this is denoted as back-supported stratification for lean conditions and yields a higher flame propagation speed [63]. Front-supported stratification, on the other hand, occurs for lean conditions when $\alpha > 90^\circ$, in this case the propagation of the flame is directed towards higher values of equivalence ratio and the flame propagation speed is thought to be lower [63]. Again, only points with a flame sensor value greater 0.01 have been taken into account, which means that a certain progress variable gradient is always ensured. However, the denominator in Eq. 21 can still become singular in regions with vanishing equivalence ratio gradients, which corresponds to perfectly premixed combustion at this point. To consider this consistently, all points with $|\nabla \phi| < 0.1$ have been collected in a separate bin. This bin is plotted above the actual plots in Fig. 21, its width is scaled to obtain a PDF peak value

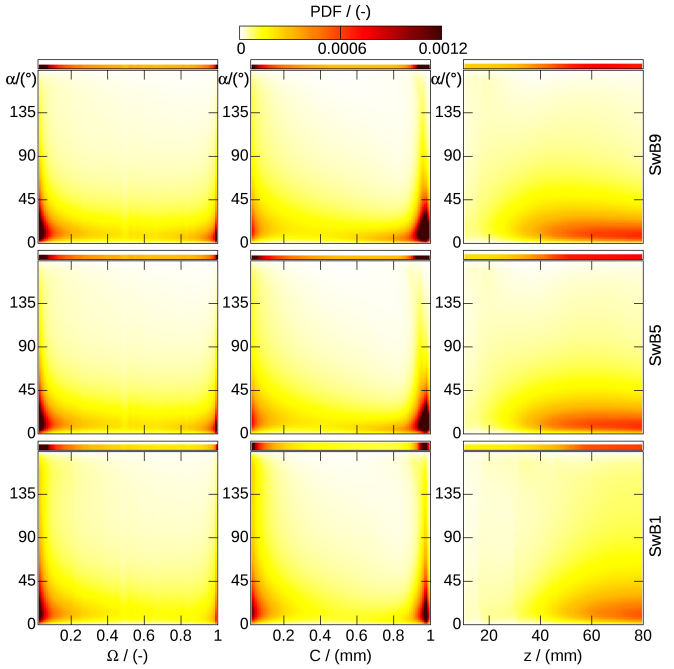

Figure 21: Joint PDFs of alignment angle between progress variable and equivalence ratio vs. Favre-filtered flame sensor (left), Favre-filtered normalized progress variable (middle) and distance from the burner exit (right).

corresponding to the rest of the plot so that the area below the PDFs can be compared.

For all cases, most of the combustion occurs in the perfectly premixed regime. Even further downstream, where the whole flame region is exposed to equivalence ratio gradients as discussed before, a significant amount of perfectly premixed combustion can be observed. This can be explained by the different magnitude of the length scales on which the combustion and the mixing process take place, so that even in a stratified region the equivalence ratio gradient inside the flame is still small in comparison to the progress variable gradient.

For SwB1, back-supported stratification can be found in the region downstream of 40 mm, mainly for low values of the flame sensor and progress variable values of either near unity or near zero. A minimal amount of front-supported stratification can also be observed, this can be explained by turbulent wrinkling, causing the flame to propagate with the equivalence ratio gradient locally.

For SwB5 and SwB9 the basic observations are comparable. The region where back-supported and small amounts of front-supported flames are found starts earlier at approximately 30 mm, as it could be expected. The amount of stratified combustion is bigger than for SwB1, especially for flame sensor values near unity. Most of the stratified combustion is found near progress variable values of unity at the burnt side of the flame for these cases.

5. Conclusions

LES computations for three different grid resolutions and stratification levels have been presented for the Cambridge stratified flame series. The ATF approach was used in combination with the FGM technique in a formulation for stratified combustion. The necessary adaptions to make the model suitable for varying mixture fractions were investigated carefully. The commonly used flame sensor formulation was replaced by a version that makes the thickening behavior independent of the mixture fraction.

Radial profiles from the simulation have been compared to measurements for mean value and fluctuations of axial and radial velocity, equivalence ratio, temperature and major species concentrations. An overall good agreement was found with some deviations occurring within the bluff body region. By analyzing atomic mass fractions and species profiles, these deviations could be assigned most likely to effects of preferential diffusion for the case SwB1 and heat transfer in the cases SwB5 and SwB9. To test the influence of the assumed sub-filter FDF, the coarse grid simulations have been carried out with and without using a top-hat distribution for the FDF in mixture fraction and progress variable, respectively. It was found that influence on the results was only small, therefore the simulations on the medium and fine grid have been performed assuming a Dirac-distribution for both mixture fraction and progress variable. Good convergence of the results with grid refinement was observed.

The overall combustion process was analyzed using contour plots, conditional PDFs and joint PDFs. It was found that combustion occurs over the whole range of equivalence ratios from the value in the respective inner stream down to the lean flammability limit. The combustion probability shows a peak at the inner stream equivalence ratio for all cases. Three different flame regions could be distinguished, first a perfectly premixed region, followed by a region in which the flame starts to burn in a stratified regime and finally a region where the unburnt side of the flames touches the lean flammability limit. The overall combustion process was found to be dominated by the contributions of the first and last region. Also in the stratified regions a large amount of the combustion takes place under quasi-premixed conditions due to a negligible equivalence ratio gradient. A significant amount of back-supported and some front-supported stratification was also found for all three cases, most dominant for SwB5 and SwB9.

Acknowledgements

The authors gratefully acknowledge funding from the state of Nordrhein-Westfalen, Germany. Computations have been carried out using the DFG supported HPC resources of the Center for Computational Sciences and Simulation (CCSS) of the University of Duisburg-Essen, Germany. We also would like to thank Robert S. Barlow, Saravanan Balusamy, Matthew J. Dunn, Simone Hochgreb,

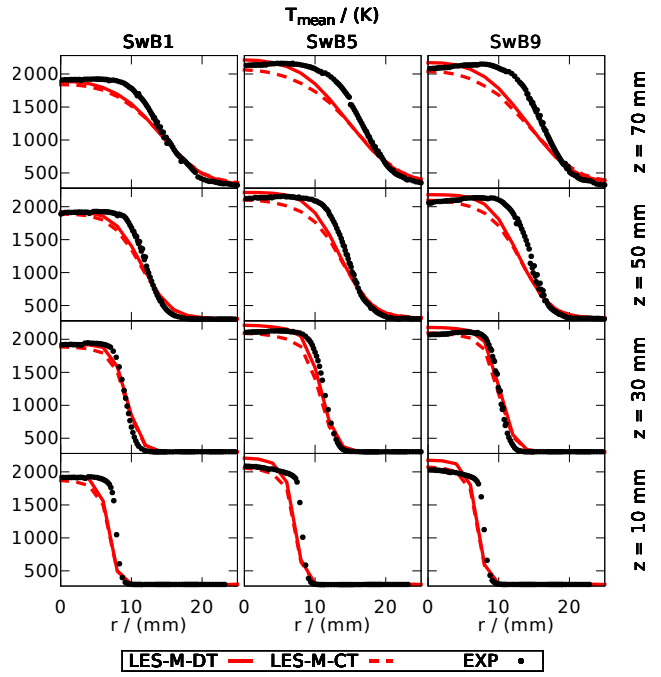

Figure A.22: Comparison of the radial mean profiles of temperature obtained with the classical ATF model with constant thickening factor F (LES-M-CT) and the applied version of the model with F determined from Eq. 7 (LES-M-DT) on the medium grid.

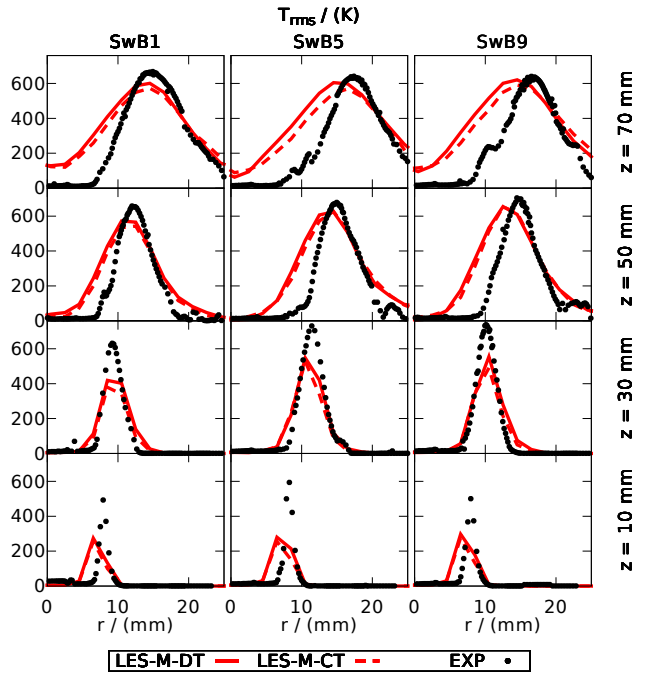

Figure A.23: Comparison of the radial fluctuation profiles of temperature obtained with the classical ATF model with constant thickening factor F (LES-M-CT) and the applied version of the model with F determined from Eq. 7 (LES-M-DT) on the medium grid.

Mark S. Sweeney and Ruigang Zhou for providing the experimental data and the TNF-community for many helpful discussions.

Appendix A. Effect of the flame sensor

Figures A.22 and A.23 show comparisons of the mean and rms temperature profiles obtained on the medium grid for a simulation with a constant thickening factor (LES-M-CT) and one with the thickening factor determined with the use the flame sensor from Eq. 7 (LES-M-DT). The overall position of the flame is not influenced by the type of thickening procedures applied. However, the structure of the burnout zone is affected. The shape of the temperature profiles in the burnout zone is in notable better agreement with the measurements for LES-M-DT. For the constant thickening factor simulation LES-M-CT, the effect of the excessive thickening of the burnout zone becomes visible, most obviously for the stratified cases SwB5 and SwB9. The excessive thickening also causes a certain under-prediction of the fluctuation level for LES-M-CT. Figure A.24 compares instantaneous snapshots of the resulting temperature field for both methods. The method with the flame sensor (LES-M-DT) reduces the flame thickness and thereby avoids excessive damping of smaller flame structures in comparison to the classical ATF model (LES-M-CT).

Appendix B. Velocity fluctuations and fitted efficiency function

The velocity fluctuations in Eq. 9 are evaluated from the correlation given by Colin et al. [8] and modified by Wang et al. [47] to work for other values than 10 for the numbers of grid points n to resolve the flame thickness:

$$\begin{aligned} u'_\Delta &= 2\Delta_{mesh}^3 \left|\nabla^2\left(\nabla\times\tilde{\vec{u}}\right)\right| \left(\frac{n}{10}\right)^{\frac{1}{3}} \\ &= 2\Delta_{mesh}^3 \left|\nabla\times\left(\nabla^2\tilde{\vec{u}}\right)\right| \left(\frac{n}{10}\right)^{\frac{1}{3}} \end{aligned} \tag{B.1}$$

The Laplace operator is evaluated on a $(4\Delta_{mesh})$ stencil, to not consider the highest frequencies (noise) [8]. The turbulent Reynolds number on the sub-filter scale is evaluated from [9]:

$$Re_\Delta = 4F_{max}\frac{u'_\Delta}{s_l^0} \tag{B.2}$$

and the fitted efficiency function from [9]:

$$\Gamma_\Delta\left(F_{max}, \frac{u'_\Delta}{s_l^0}, Re_\Delta\right) = \left[\left\{\left(f_u^{-a} + f_\Delta^{-a}\right)^{-\frac{1}{a}}\right\}^{-b} + f_{Re}^{-b}\right]^{-\frac{1}{b}} \tag{B.3}$$

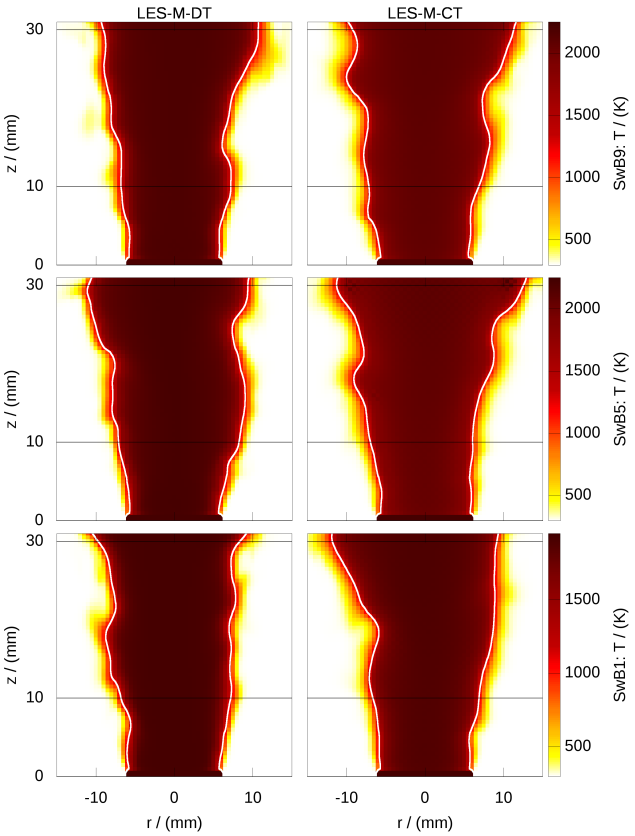

Figure A.24: Comparison of instantaneous contour plots of temperature obtained with the classical ATF model with constant thickening factor F (LES-M-CT) and the applied version of the model with F determined from Eq. 7 (LES-M-DT) on the medium grid. The white isolines mark a progress variable value of $C = 0.5$.

with

$$f_u = 4\left(\frac{27C_k}{110}\right)^{\frac{1}{2}}\left(\frac{18C_k}{55}\right)\left(\frac{u'_\Delta}{s_l^0}\right)^2 \tag{B.4}$$

$$f_\Delta = \left[\frac{27C_k\pi^{\frac{4}{3}}}{110}\left\{(F_{max})^{\frac{4}{3}} - 1\right\}\right]^{\frac{1}{2}} \tag{B.5}$$

$$f_{Re} = \left[\frac{9}{55}\exp\left(-\frac{3}{2}C_k\pi^{\frac{4}{3}}Re_\Delta^{-1}\right)\right]^{\frac{1}{2}} Re_\Delta^{\frac{1}{2}} \tag{B.6}$$

$$a = 0.6 + 0.2\,\exp\left(-0.1\frac{u'_\Delta}{s_l^0}\right) - 0.2\,\exp\left(-0.01\;F_{max}\right) \tag{B.7}$$

$$b = 1.4 \tag{B.8}$$

where $C_k = 1.5$ is the Kolmogorov constant. It was found that the evaluation of this efficiency function became computationally expensive in comparison to the rest of the CFD solver, consuming up to 25% of the runtime. A significant speedup was achieved by tabulating Eq. 9 at the beginning of the computation, and then obtaining the value of E from an additional table lookup depending on the local value of the maximum thickening factor and the velocity ratio.

Appendix C. Variance modeling

For a one-dimensional case, the gradient model for the mixture fraction by Branley and Jones [51] reads:

$$\widetilde{Z''^2} = C_2\Delta^2\left(\frac{Z_N - Z_S}{2\Delta}\right)^2 , \tag{C.1}$$

where Z_N and Z_S represent the values at the neighboring cell centers. Floyd et al. [48] have shown that in cases of a linear mixture fraction profile, the resulting value of the modeling constant is:

$$C_2 = \frac{1}{12} , \tag{C.2}$$

which results in in a upper and lower limit of:

$$\tilde{Z}_{u/l} = \tilde{Z} \pm 0.5\sqrt{12\widetilde{Z''^2}} = \tilde{Z} \pm 0.25(Z_N - Z_S) \tag{C.3}$$

For the approach used within this work, the values at the cell faces are obtained from the mean value of the neighboring cells

$$Z_s = 0.5(Z_S + Z_C) \text{ and } Z_n = 0.5(Z_N + Z_C) \tag{C.4}$$

where Z_c denotes the value at the cell center. The gradient over the cell is then obtained from

$$\frac{dZ}{dx} = \frac{Z_n - Z_s}{\Delta} = \frac{Z_N - Z_S}{2\Delta} \tag{C.5}$$

This results in an upper and lower limit of :

$$\tilde{Z}_{u/l} = \tilde{Z} \pm 0.5\Delta\frac{dZ}{dx} = \tilde{Z} \pm 0.25(Z_N - Z_S) \tag{C.6}$$

which is in agreement with the result for the gradient assumption in Eq. C.3.

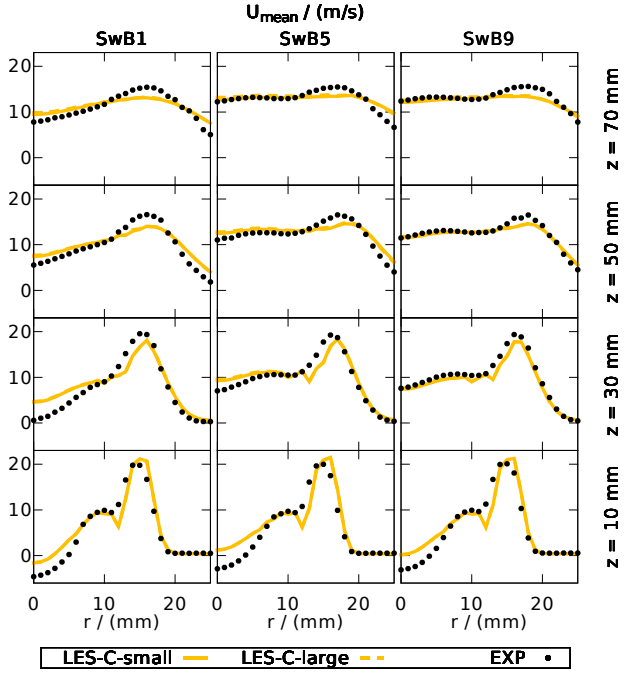

Figure D.25: Investigation of the influence of the domain size on the radial mean profiles of axial velocity.

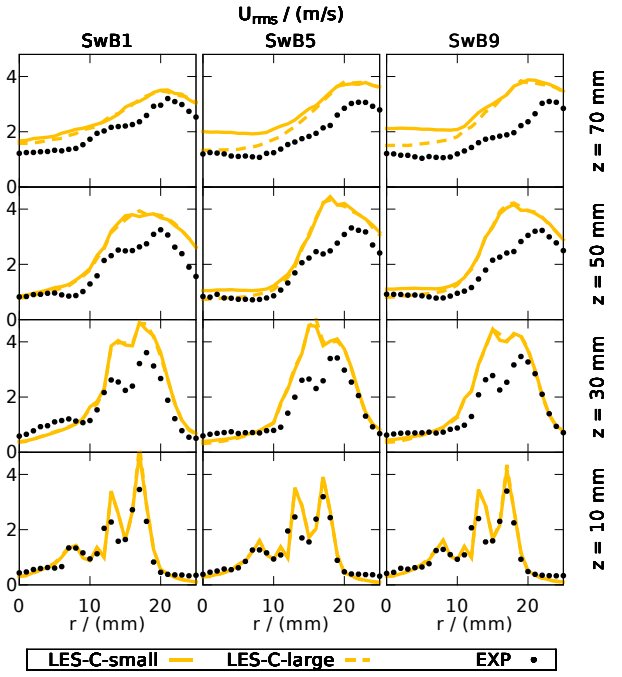

Figure D.26: Investigation of the influence of the domain size on the radial fluctuation profiles of axial velocity.

Appendix D. Influence of domain size

To study the influence of the domain size, additional computations were carried out for the coarse grid on a domain that had doubled size in all directions. The influence on the mean values of all quantities was found to be negligible, Fig. D.25 shows the respective comparison for axial velocity as an example. Some deviations occurred for the fluctuations of axial velocity further downstream, as displayed in Fig. D.26. For all other quantities the deviations in the fluctuations were negligible, some example profiles 70 mm above the burner are shown in Fig. D.27. Therefore, it was decided to choose the smaller domain, as the simulation results benefit significantly from the finer resolution that is computational affordable on the smaller domain.

Appendix E. Comparison of thickening and filtering

The ATF model with flame sensor used in this work is compared to the filtering procedure that forms the basis of approaches like the F-TACLES [30] or the (FLF) - PDF model [32] in this section. For that purpose, a one-dimensional flame computation for stoichiometric conditions has been carried out with Cantera. The resulting profiles for the mass fractions of progress variable (product species), methane (educt species) and carbon monoxide (intermediate species) as well as for the temperature have been stored over the flame normal coordinate (Original). Afterwards, these profiles have been filtered with

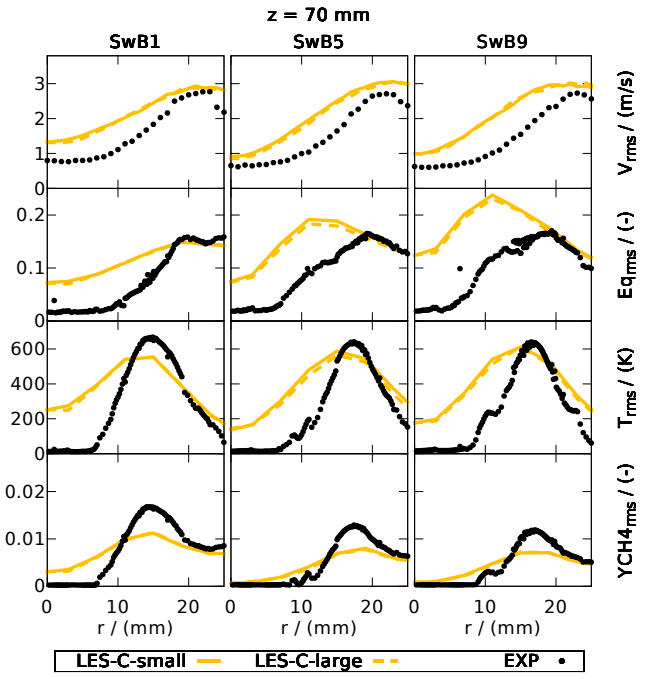

Figure D.27: Investigation of the influence of the domain size on the radial fluctuation profiles of selected quantities 70 mm above the burner.

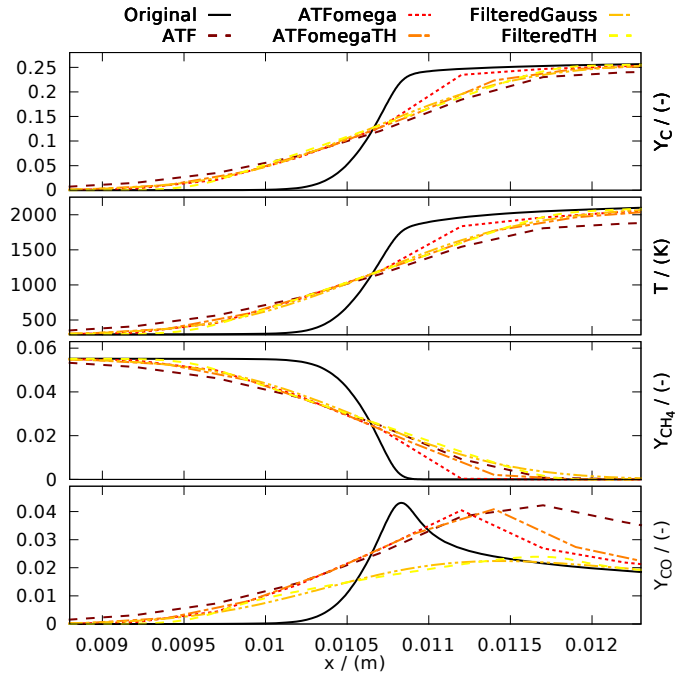

Figure E.28: Comparison of the influence of thickening and filtering on the structure of a one-dimensional flame.

a top-hat filter (FilteredTH, $\Delta = 2.2$ mm) and a Gaussian filter (FilteredGaussian, $\Delta = 6.0$ mm), respectively. Afterwards 'PsiPhi' was used to simulated a laminar one-dimensional flame on a 0.5 mm grid with the classical ATF-model (ATF, constant thickening factor of 5), the ATF-model with flame sensor (ATFomega) and the ATF-model with flame sensor and top-hat FDF in C (ATFomegaTH). The respective comparison is shown in Fig. E.28, except for the intermediate species similar results are achieved for the different approaches. The influence of the thickening procedure on the pre-heat and burnout zone for the ATF-model without flame sensor becomes obvious. It is notable that the top-hat FDF improves the agreement with the filtered results significantly in the burnout zone, and has negligible influence at the unburnt side of the flame. For the intermediate species carbon monoxide, the filtering procedure preserves the area below the profile and under-predicts its peak value, whereas the thickening procedure preserves the peak value and over-predicts the area below the profile.

Appendix F. Mean and rms profiles of major species mass fractions

The radial profiles of mass fraction means and fluctuations for major species are shown in Figures F.29-F.38.

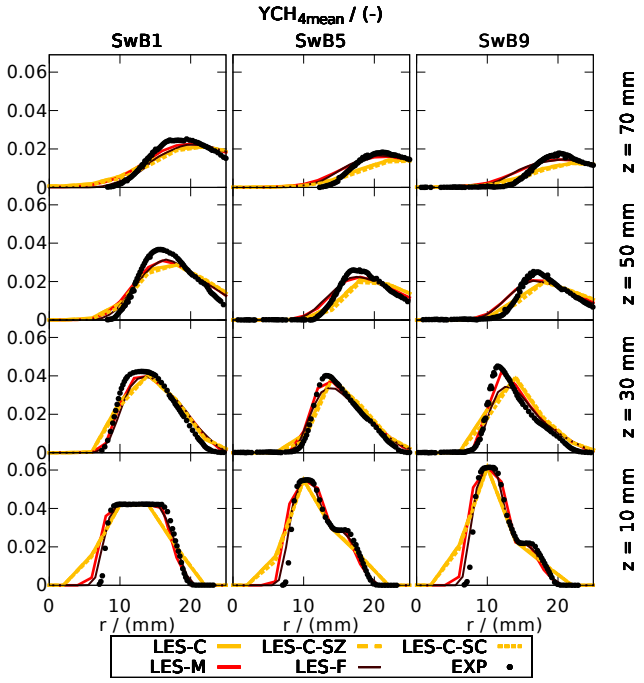

Figure F.29: Radial profiles of the mean methane mass fraction at different downstream locations, showing a comparison for three different grids with the experiments. LES-C-SZ and LES-C-SC refer to a coarse grid simulation with additional sub-filter modeling using a top-hat FDF in mixture fraction and progress variable, respectively.

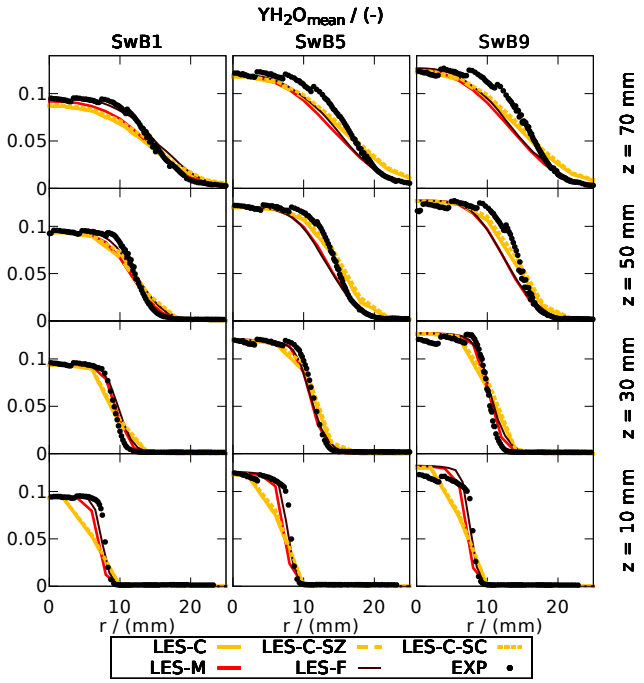

Figure F.30: Radial profiles of the mean water mass fraction at different downstream locations, showing a comparison for three different grids with the experiments. LES-C-SZ and LES-C-SC refer to a coarse grid simulation with additional sub-filter modeling using a top-hat FDF in mixture fraction and progress variable, respectively.

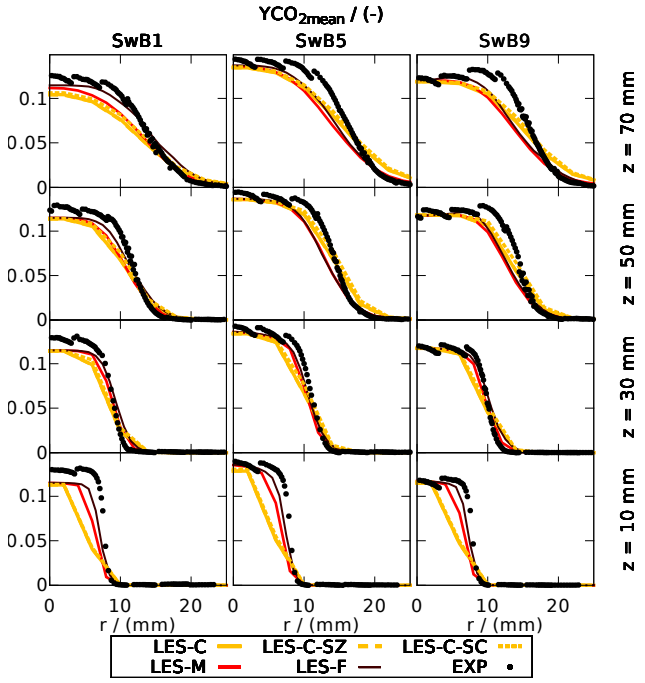

Figure F.31: Radial profiles of the mean carbon dioxide mass fraction at different downstream locations, showing a comparison for three different grids with the experiments. LES-C-SZ and LES-C-SC refer to a coarse grid simulation with additional sub-filter modeling using a top-hat FDF in mixture fraction and progress variable, respectively.

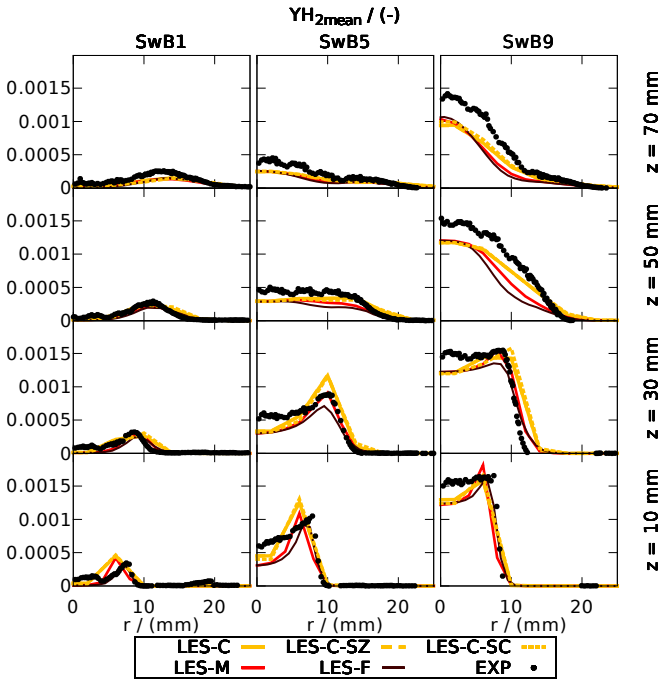

Figure F.33: Radial profiles of the mean hydrogen mass fraction at different downstream locations, showing a comparison for three different grids with the experiments. LES-C-SZ and LES-C-SC refer to a coarse grid simulation with additional sub-filter modeling using a top-hat FDF in mixture fraction and progress variable, respectively.

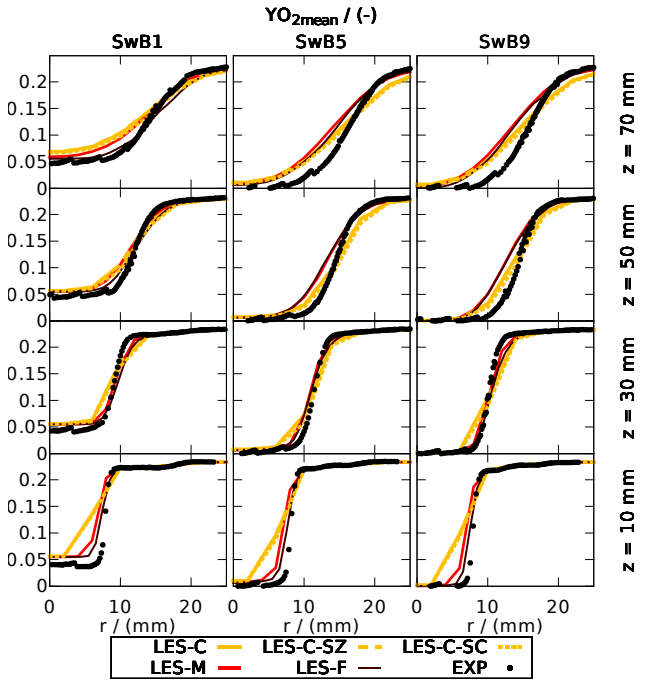

Figure F.32: Radial profiles of the mean oxygen mass fraction at different downstream locations, showing a comparison for three different grids with the experiments. LES-C-SZ and LES-C-SC refer to a coarse grid simulation with additional sub-filter modeling using a top-hat FDF in mixture fraction and progress variable, respectively.

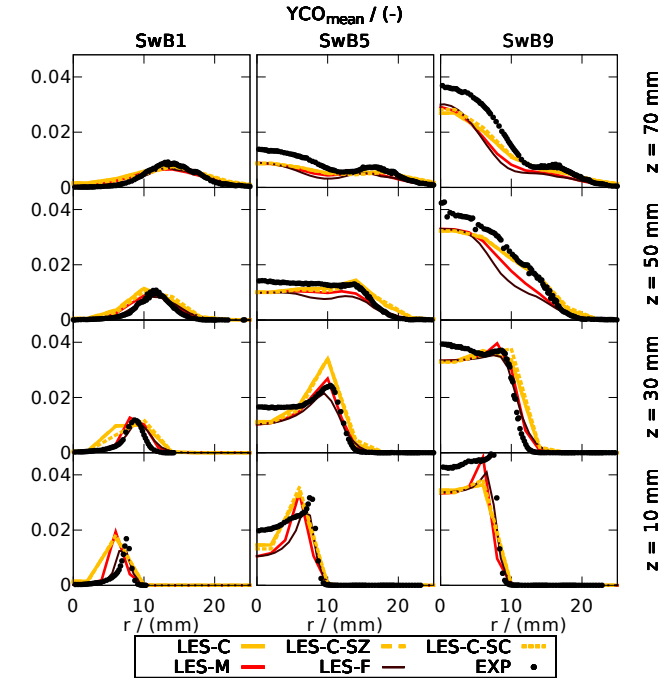

Figure F.34: Radial profiles of the mean carbon monoxide mass fraction at different downstream locations, showing a comparison for three different grids with the experiments. LES-C-SZ and LES-C-SC refer to a coarse grid simulation with additional sub-filter modeling using a top-hat FDF in mixture fraction and progress variable, respectively.

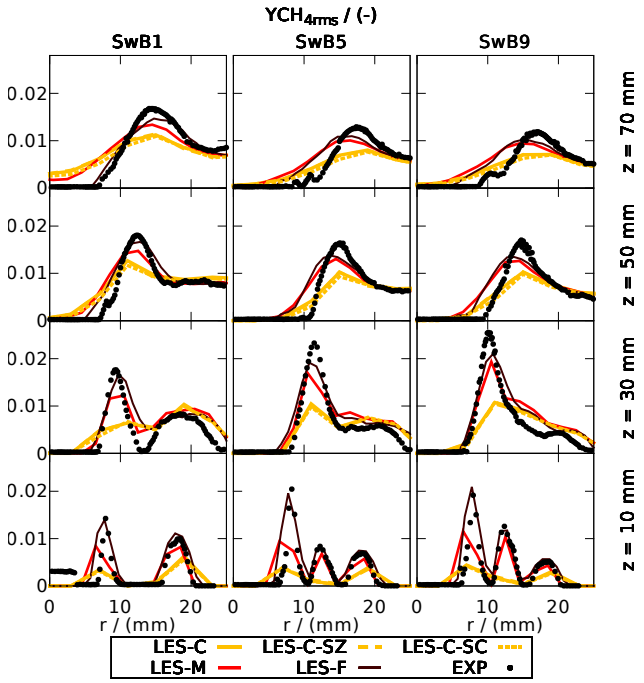

Figure F.35: Radial profiles of the methane mass fraction fluctuations at different downstream locations, showing a comparison for three different grids with the experiments. LES-C-SZ and LES-C-SC refer to a coarse grid simulation with additional sub-filter modeling using a top-hat FDF in mixture fraction and progress variable, respectively.

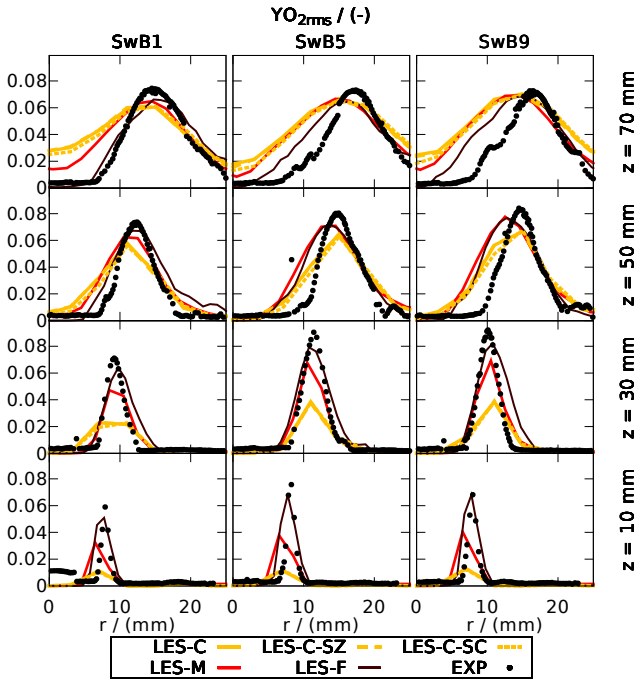

Figure F.37: Radial profiles of the oxygen mass fraction fluctuations at different downstream locations, showing a comparison for three different grids with the experiments. LES-C-SZ and LES-C-SC refer to a coarse grid simulation with additional sub-filter modeling using a top-hat FDF in mixture fraction and progress variable, respectively.

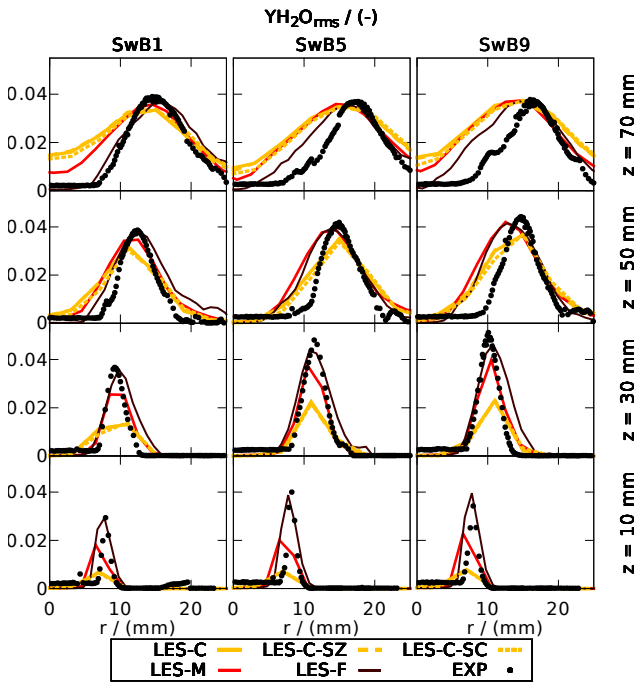

Figure F.36: Radial profiles of the water mass fraction fluctuations at different downstream locations, showing a comparison for three different grids with the experiments. LES-C-SZ and LES-C-SC refer to a coarse grid simulation with additional sub-filter modeling using a top-hat FDF in mixture fraction and progress variable, respectively.

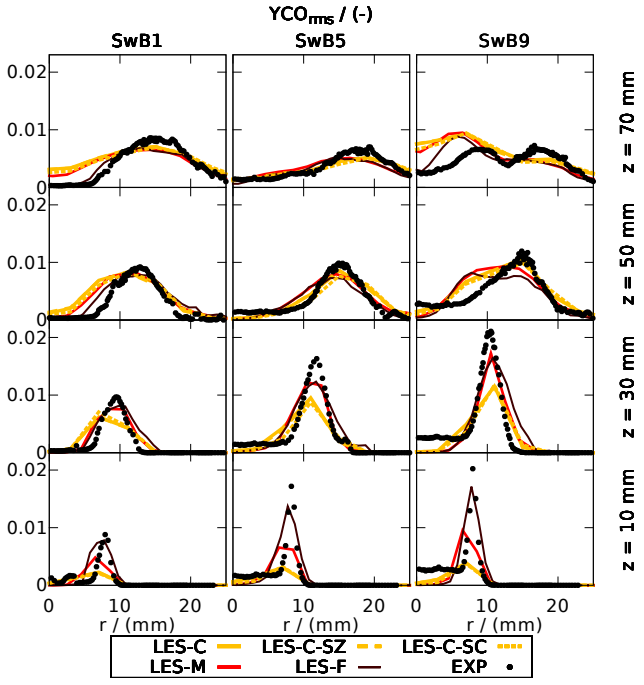

Figure F.38: Radial profiles of the carbon monoxide mass fraction fluctuations at different downstream locations, showing a comparison for three different grids with the experiments. LES-C-SZ and LES-C-SC refer to a coarse grid simulation with additional sub-filter modeling using a top-hat FDF in mixture fraction and progress variable, respectively.

References

[1] M. S. Sweeney, S. Hochgreb, M. J. Dunn, R. S. Barlow, Combust. Flame 159 (2012) 2896–2911.

[2] M. S. Sweeney, S. Hochgreb, M. J. Dunn, R. S. Barlow, Combust. Flame 159 (2012) 2912–2929.

[3] N. Peters, Turbulent Combustion, Cambridge University Press, 2000.

[4] H. Pitsch, Combust. Flame 143 (2005) 587–598.

[5] M. Düsing, A. M. Kempf, F. Flemming, A. Sadiki, J. Janicka, Prog. Comp. Fluid Dyn. 5 (2005) 363–374.

[6] V. Moureau, B. Fiorina, H. Pitsch, Combust. Flame 156 (2009) 801–812.

[7] T. D. Butler, P. J. O'Rourke, Proc. Combust. Inst. 16 (1977) 1503–1515.

[8] O. Colin, F. Ducros, D. Veynante, T. Poinsot, Phys. Fluids 12 (2000) 1843–1863.

[9] F. Charlette, C. Meneveau, D. Veynante, Combust. Flame 131 (2002) 159–180.

[10] M. Boger, D. Veynante, H. Boughanem, A. Trouve, Proc. Combust. Inst. 27 (1998) 917–925.

[11] K. N. C. Bray, J. B. Moss, Acta Aeronautica 4 (1977) 219–319.

[12] C. Angelberger, D. Veynante, F. Egolfopoulos, T. Poinsot, in: Proceedings of the Summer Programm, Center for Turbulence Research, Stanford, pp. 61–82.

[13] C. Fureby, Proc. Combust. Inst. 30 (2005) 593–601.

[14] S. P. R. Muppala, N. K. Aluri, F. Dinkelacker, A. Leipertz, Combust. Flame 140 (2005) 257–266.

[15] T. Ma, O. Stein, N. Chakraborty, A. M. Kempf, Combust. Theory Model. 17 (2013) 431–482.

[16] T. Ma, O. T. Stein, N. Chakraborty, A. M. Kempf, Combust. Theory Model. 18 (2014) 32–64.

[17] U. Maas, S. B. Pope, Combust. Flame 88 (1992) 239–264.

[18] O. Gicquel, N. Darabiha, D. Thévenin, Proc. Combust. Inst. 28 (2000) 1901–1908.

[19] B. Fiorina, O. Gicquel, L. Vervisch, S. Carpentier, N. Darabiha, Combust. Flame 140 (2005) 147–160.

[20] J. A. van Oijen, L. P. H. de Goey, Combust. Sci. Technol. 161 (2000) 113–137.

[21] J. A. van Oijen, R. J. M. Bastiaans, L. P. H. de Goey, Proc. Combust. Inst. 31 (2007) 1377–1384.

[22] A. W. Vreman, B. A. Albrecht, J. A. van Oijen, L. P. H. de Goey, R. J. M. Bastiaans, Combust. Flame 153 (2008) 394–416.

[23] G. Kuenne, A. Ketelheun, J. Janicka, Combust. Flame 158 (2011) 1750–1767.

[24] J. Galpin, A. Naudin, L. Vervisch, C. Angelberger, O. Colin, P. Domingo, Combust. Flame 155 (2008) 247–266.

[25] B. Fiorina, R. Vicquelin, P. Auzillon, N. Darabiha, O. Gicquel, D. Veynante, Combust. Flame 157 (2010) 465–475.

[26] G. Kuenne, F. Seffrin, F. Fuest, T. Stahler, A. Ketelheun, D. Geyer, J. Janicka, A. Dreizler, Combust. Flame 159 (2012) 2669–2689.

[27] F. C. Marincola, T. Ma, A. M. Kempf, Proc. Combust. Inst. 34 (2013) 1307–1315.

[28] P. Trisjono, K. Kleinheinz, H. Pitsch, S. Kang, Flow Turbul. Combust. 92 (2014) 201–235.

[29] F. Seffrin, F. Fuest, D. Geyer, A. Dreizler, Combust. Flame 157 (2010) 384–396.

[30] P. Auzillon, O. Gicquel, N. Darabiha, D. Veynante, B. Fiorina, Combust. Flame 159 (2012) 2704–2717.

[31] B. Janus, A. Dreizler, J. Janicka, Proc. Combust. Inst. 31 (2007) 3091–3098.

[32] S. Nambully, P. Domingo, V. Moureau, L. Vervisch, Combust. Flame (2014) `http://dx.doi.org/10.1016/j.combustflame.2014.01.005`.

[33] S. Nambully, P. Domingo, V. Moureau, L. Vervisch, Combust. Flame (2014) `http://dx.doi.org/10.1016/j.combustflame.2014.01.006`.

[34] D. G. Goodwin, Cantera: An object-oriented software toolkit for chemical kinetics, thermodynamics, and transport processes, `http://code.google.com/p/cantera`, 2009.

[35] G. P. Smith, D. M. Golden, M. Frenklach, N. W. Moriarty, B. Eiteneer, M. Goldenberg, C. T. Bowman, R. K. Hanson, S. Song, W. C. Gardiner, Jr., V. V. Lissianski, Z. Qin, `http://www.me.berkeley.edu/gri_mech`, 2000.

[36] M. Ihme, L. Shunn, J. Zhang, J. Comput. Phys. 231 (2012) 7715–7721.

[37] Y.-S. Niu, L. Vervisch, P. D. Tao, Combust. Flame 160 (2013) 776–785.

[38] T. Poinsot, D. Veynante, Theoretical and Numerical Combustion, Aquaprint, Bordeaux, France, 3rd edition, 2012.

[39] H. Pitsch, H. Steiner, Phys. Fluids 12 (2000) 2541–2554.

[40] J. Lamouroux, M. Ihme, B. Fiorina, O. Gicquel, Combust. Flame (2014) `http://dx.doi.org/10.1016/j.combustflame.2014.01.015`.

[41] A. Ketelheun, G. Kuenne, J. Janicka, Flow Turbul. Combust. 91 (2013) 867–893.

[42] R. W. Bilger, S. H. Stårner, R. J. Kee, Combust. Flame 80 (1990) 135–149.

[43] Y. Shoshin, L. Tecce, J. Jarosinski, Combust. Sci. Technol. 180 (2008) 1812–1828.

[44] E. V. Lavante, R. A. Strehlow, Combust. Flame 49 (1983) 123–140.

[45] J. P. Legier, T. Poinsot, D. Veynante, in: Proceedings of the Summer Programm, Center for Turbulence Research, Stanford, pp. 157–168.

[46] L. Durand, W. Polifke, in: Turbo Expo, ASME, 2007.

[47] G. Wang, M. Boileau, D. Veynante, Combust. Flame 158 (2011) 2199–2213.

[48] J. Floyd, A. M. Kempf, A. Kronenburg, R. H. Ram, Combust. Theory Mod. 13 (2009) 559–588.

[49] C. Olbricht, O. T. Stein, J. Janicka, J. A. van Oijen, S. Wysocki, A. M. Kempf, Fuel 96 (2012) 100–107.

[50] A. W. Vreman, J. A. Oijen, L. P. H. DeGoey, R. J. M. Bastiaans, Flow Turbul. Combust. 82 (2009) 511–535.

[51] N. Branley, W. P. Jones, Combust. Flame 127 (2001) 1914–1934.

[52] R. Zhou, S. Balusamy, M. S. Sweeney, R. S. Barlow, S. Hochgreb, Combust. Flame 160 (2013) 2017–2028.

[53] M. Pettit, B. Coriton, A. Gomez, A. M. Kempf, Proc. Combust.Inst. 33 (2011) 1391–1399.

[54] A. M. Kempf, B. Geurts, J. C. Oefelein, Combust. Flame 158 (2011) 2408–2419.

[55] G. Zhou, Numerical simulations of physical discontinuities in single and multi-fluid flows for arbitrary Mach numbers, Ph.D. thesis, Chalmers University of Technology, Goteborg, Sweden, 1995.

[56] F. Nicoud, H. B. Toda, O. Cabrit, S. Bose, J. Lee, Phys. Fluids 23 (2011) 085106.

[57] M. Klein, A. Sadiki, J. Janicka, J. Comput. Phys. 186 (2003) 652–665.

[58] A. M. Kempf, S. Wysocki, M. Pettit, Comput. Fluids 60 (2012) 58–60.

[59] H. Yamashita, M. Shimada, T. Takeno, Proc. Combust. Inst. 26 (1996) 27–34.

[60] R. S. Barlow, M. J. Dunn, M. S. Sweeney, S. Hochgreb, Combust. Flame 159 (2012) 2563–2575.

[61] M. J. Dunn, R. S. Barlow, Proc. Combust. Inst. 34 (2013) 1411–1419.

[62] V. Katta, W. M. Roquemore, Proc. Combust. Inst. 34 (2013) 1101–1108.

[63] A. P. D. Cruz, A. M. Dean, J. M. Grenda, Proc. Combust. Inst. 28 (2000) 1925–1932.